


Cite this: *RSC Adv.*, 2025, 15, 14477

New nicotinamide–thiadiazol hybrids as VEGFR-2 inhibitors for breast cancer therapy: design, synthesis and *in silico* and *in vitro* evaluation†

Walid E. Elgammal,^a Hazem Elkady,^{a,b} Reda G. Yousef,^{bc} Wagdy M. Eldehna,^{de} Dalal Z. Husein,^f Fatma G. Amin,^g Bshra A. Alsouk,^h Eslam B. Elkaeed,ⁱ Ibrahim H. Eissa^{a,b} and Ahmed M. Metwaly^{a,j}

Vascular endothelial growth factor receptor-2 (VEGFR-2) is a key regulator of tumor angiogenesis and has become an important target in anticancer drug development. In this study, novel nicotinamide–thiadiazol hybrids were synthesized and evaluated for their anti-breast cancer potential through VEGFR-2 inhibition. The compounds were assessed *in vitro* for their cytotoxicity against MDA-MB-231 and MCF-7 cell lines. Among the nicotinamide–thiadiazol hybrids, **7a** exhibited the most potent anticancer activity, with IC₅₀ values of 4.64 ± 0.3 μM in MDA-MB-231 and 7.09 ± 0.5 μM in MCF-7, showing comparable efficacy to sorafenib. VEGFR-2 inhibition assays confirmed strong inhibitory potential with an IC₅₀ of 0.095 ± 0.05 μM. *In vitro* cell cycle analysis indicated that **7a** induced S-phase arrest, while apoptosis assays demonstrated a substantial increase in late apoptotic cells (44.01%). Other *in vitro* mechanistic studies further confirmed the activation of the intrinsic apoptotic pathway, as evidenced by caspase-3 activation (8.2-fold), Bax upregulation (6.9-fold), and Bcl-2 downregulation (3.68-fold). Computational studies, including molecular docking and 200 ns molecular dynamics (MD) simulations, confirmed the stable interaction of **7a** with VEGFR-2, showing binding affinities comparable to sorafenib. Further validation through MM-GBSA, ProLIF, PCAT, and FEL analyses reinforced its strong binding capability. Additionally, ADMET predictions suggested favorable pharmacokinetic properties, including good absorption, high plasma protein binding, and non-CYP2D6 inhibition. Moreover, toxicity analysis classified **7a** as non-mutagenic and non-carcinogenic, with a lower predicted toxicity than sorafenib. Finally, density functional theory (DFT) calculations highlighted the structural stability and reactivity of **7a**, further supporting its potential as a VEGFR-2 inhibitor. These findings suggest that **7a** is a promising VEGFR-2 inhibitor with significant anticancer potential, favorable pharmacokinetics, and an improved safety profile. Further preclinical studies and structural modifications are warranted to optimize its therapeutic potential.

Received 19th February 2025
Accepted 22nd April 2025

DOI: 10.1039/d5ra01223f

rsc.li/rsc-advances

1. Introduction

Cancer remains a leading cause of mortality worldwide,^{1,2} with breast cancer being the most frequently diagnosed malignancy among women. Despite significant advances in cancer treatment, the development of resistance to conventional chemotherapeutic agents and targeted therapies presents a major

challenge in clinical oncology. Angiogenesis, the process of forming new blood vessels, plays a crucial role in tumor growth, progression, and metastasis.³ Among the various pro-angiogenic factors, VEGFR-2 is a key mediator of endothelial cell proliferation, migration, and survival, making it an attractive therapeutic target for antiangiogenic drug development.^{4,5}

^aChemistry Department, Faculty of Science, Al-Azhar University, Nasr City, 11884, Cairo, Egypt

^bPharmaceutical Medicinal Chemistry & Drug Design Department, Faculty of Pharmacy (Boys), Al-Azhar University, Cairo, 11884, Egypt. E-mail: Ibrahim.eissa@azhar.edu.eg; Hazemelkady@azhar.edu.eg

^cPharmaceutical Chemistry Department, Faculty of Pharmacy, Merit University, Sohag 82755, Egypt

^dDepartment of Pharmaceutical Chemistry, Faculty of Pharmacy, Kafrelsheikh University, P. O. Box 33516, Kafrelsheikh, Egypt

^eDepartment of Pharmaceutical Chemistry, Faculty of Pharmacy, Pharos University in Alexandria, Canal El Mahmoudia Street, Alexandria 21648, Egypt

^fChemistry Department, Faculty of Science, New Valley University, El-Kharja, 72511, Egypt

^gPhysics Department, Faculty of Science, Alexandria University, Alexandria, Egypt

^hDepartment of Pharmaceutical Sciences, College of Pharmacy, Princess Nourah bint Abdulrahman University, P. O. Box 84428, Riyadh 11671, Saudi Arabia

ⁱDepartment of Pharmaceutical Sciences, College of Pharmacy, AlMaarefa University, P.O. Box 71666, Riyadh 11597, Saudi Arabia

^jPharmacognosy and Medicinal Plants Department, Faculty of Pharmacy (Boys), Al-Azhar University, Cairo 11884, Egypt. E-mail: ametwaly@azhar.edu.eg

† Electronic supplementary information (ESI) available. See DOI: <https://doi.org/10.1039/d5ra01223f>



Several VEGFR-2 inhibitors, including sorafenib, sunitinib, and pazopanib, have been approved for the treatment of various cancers.⁶ These inhibitors function by blocking the VEGF/VEGFR-2 signaling cascade, thereby reducing angiogenesis and limiting tumor growth.⁷ However, despite their clinical success, many of these agents are associated with significant drawbacks, including acquired resistance,^{8,9} off-target toxicities,^{10–12} and suboptimal pharmacokinetic properties.¹³ These limitations highlight the need for novel VEGFR-2 inhibitors with improved efficacy, selectivity, and safety profiles.

Nicotinamide, a derivative of vitamin B3, has gained considerable attention in drug discovery due to its diverse biological activities, including anticancer effects. Nicotinamide-based scaffolds have been explored as promising leads for kinase inhibitors, including those targeting VEGFR-2, due to their ability to form key interactions with the ATP-binding site of the receptor.¹⁴ Likewise, thiadiazole moieties are widely recognized for their ability to fight cancer by interactions with target proteins.¹⁵

Computational chemistry plays a crucial role in modern drug discovery, transforming how new medicines are designed and improved.¹⁶ Using advanced algorithms and molecular modeling, enables the prediction of how drugs interact with biological targets at the atomic level, saving both time and money compared to traditional experiments.¹⁷ Techniques like molecular docking, and MD simulations help evaluate how well drugs bind to their targets shedding light on the relationship between a compound's structure and its activity, guiding smarter drug design and refinement.^{18,19} ADMET predictions (covering absorption, distribution, metabolism, excretion, and toxicity) allow assessment of pharmacokinetics and safety early in development.^{20,21} By combining computational methods with lab experiments, drug discovery becomes more accurate and efficient, leading to better treatments for challenging targets like infections^{22,23} and cancer.^{24,25}

Our team has successfully identified and developed a range of nicotinamide^{26–28} and thiadiazole^{29–32} derivatives that act as potent VEGFR-2 inhibitors and significant potential anti-cancer agents. Merging these two pharmacophores enables the development and synthesis of innovative hybrids capable of selectively inhibiting VEGFR-2 and demonstrating strong anticancer properties. The compounds were examined *in vitro* and *in silico* for their anticancer and VEGFR-2 inhibition.

1.1. Rationale

The ATP-binding site of VEGFR-2 consists of several distinct pockets, such as the hinge region, the linker region between the hinge and DFG domain, the DFG region, and an allosteric hydrophobic pocket (Fig. 1). VEGFR-2 inhibitors (**I** and **II**) typically display essential pharmacophoric characteristics: (i) a hetero-aromatic group that forms hydrogen bonds with Cys919 in the hinge region, (ii) a spacer group that aligns between the hinge region and the DFG domain to maintain proper orientation, (iii) a pharmacophore group with hydrogen bond donor and acceptor properties that interact with Glu885 and Asp1046 in the DFG domain, and (iv) a hydrophobic tail

that binds to the allosteric hydrophobic pocket of the ATP-binding site.^{33–36}

Recently, our research team discovered several nicotinamide compounds (**III** (ref. 37) and **IV** (ref. 38)) (Fig. 1) as highly effective VEGFR-2 inhibitors. Compound **III** showed promising IC₅₀ values of 2.1, 4.61, and 4.05 μM against MCF-7, HepG2, and HCT-116 cell lines, respectively. Its activities was stronger than those of sorafenib (IC₅₀ = 6.72, 7.40, and 9.30 μM against MCF-7, HepG2, and HCT-116, respectively). The cytotoxic activity of compound **IV** against HCT-116 cells (IC₅₀ = 3.08 μM) was almost double that of sorafenib (IC₅₀ = 7.28 μM), while its activity against HepG-2 (IC₅₀ = 4.09 μM) was about 1.2-fold more than sorafenib (IC₅₀ = 5.28 μM). Compounds **III** and **IV** exhibited good VEGFR-2 inhibitory activities with IC₅₀ values of 240 and 24.93 nM (Fig. 1).

In this study, compounds **III** and **IV** served as lead structures for further modifications aimed at developing more potent VEGFR-2 inhibitors. The nicotinamide scaffold (heterocyclic head) was retained. The 1-phenylethylidene linker remained unchanged. The hydrazine (pharmacophore) moiety was replaced by a 2-hydrazono-2,3-dihydro-1,3,4-thiadiazole moiety. However, the hydrophobic tail (4-nitrophenyl and phenyl groups) of compounds **III** and **IV**, respectively were replaced with different substituted phenyl rings to increase the hydrophobic interaction at the allosteric pocket (Fig. 1).

2. Results and discussions

2.1. Chemistry

This study builds on prior findings and concentrates on the synthesis of newly designed nicotinamide compounds **7a–g**. The synthesis of these compounds was conducted according to the pathways depicted in Scheme 1. Compound **3** was synthesized by the addition of nicotinoyl chloride **2** to 4-aminoacetophenone **1** under stirring in an ice bath. The produced compound **3** was subsequently refluxed with methyl hydrazinecarbodithioate **4** in absolute ethanol, yielding methyl (*E*)-2-(1-(4-(nicotinamido)phenyl)ethylidene)hydrazine-1-carbodithioate **5** in a good yield. Finally, compound **5** subsequently reacted with the hydrazono derivatives **6a–g** in ethanol under reflux conditions, utilizing triethylamine as a catalyst, resulting in the formation of the target nicotinamide derivatives **7a–g**, respectively. The IR, NMR, and CHN data provide detailed insights into the structure of the compounds. The FT-IR spectra show characteristic absorption bands that reflect key functional groups: the NH stretch around 3300 cm⁻¹, indicative of the amide or hydrazone group, along with aromatic C–H stretches in the range of 3000–3050 cm⁻¹. The C=O stretching vibrations are observed around 1650–1700 cm⁻¹, confirming the presence of a carbonyl group, and C–H aliphatic stretches are seen in the 2800–3000 cm⁻¹ region. The ¹H NMR spectra exhibit well-resolved signals, with the amide NH proton appearing as a singlet around δ 10.60–10.66 ppm. Aromatic protons are found in the δ 7–9 ppm range, with splitting patterns such as doublets (d), double doublets (dd), and multiplets (m), which suggest a highly substituted aromatic system. Additionally, the acetyl group (–COCH₃) protons appear as singlets around



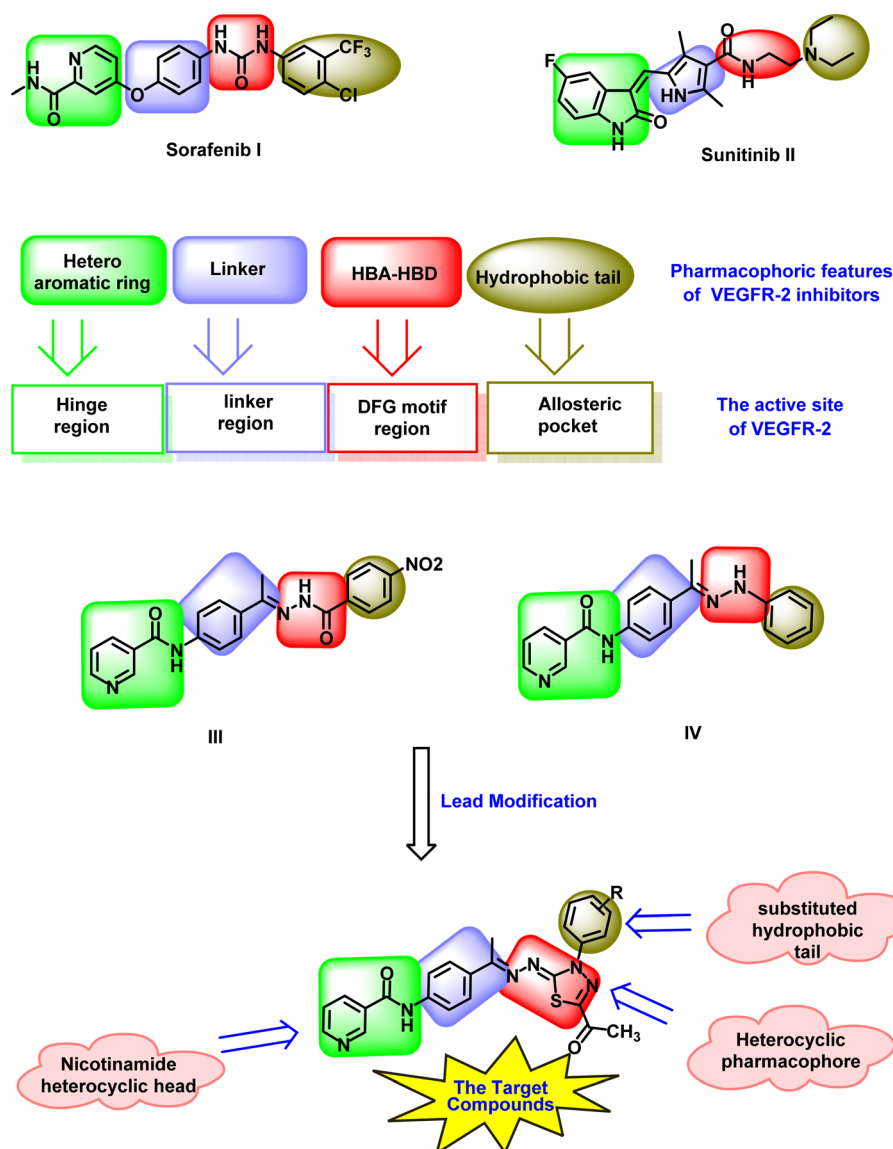


Fig. 1 Rational design of the new nicotinamide–thiadiazol hybrids as VEGFR-2 inhibitors. Sorafenib and sunitinib as examples of FDA-approved VEGFR-2 inhibitors showing the essential pharmacophoric features. Compounds III and IV as reported highly effective VEGFR-2 inhibitors. The designed compounds have the main pharmacophoric features of VEGFR-2 inhibitors.

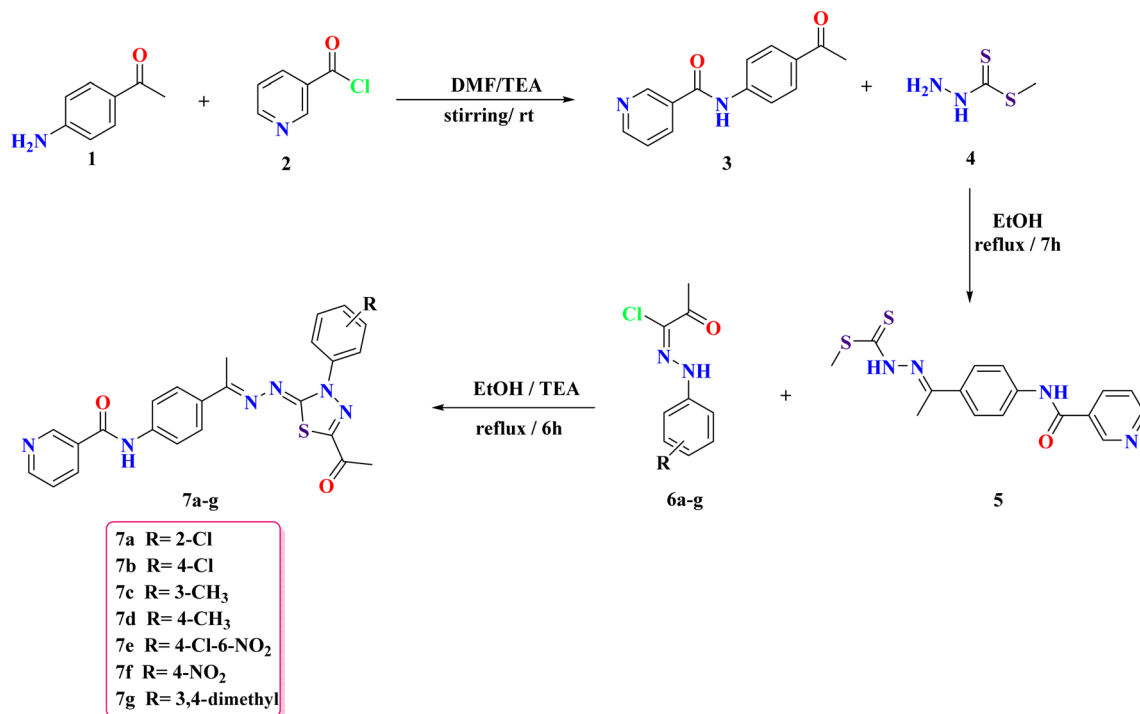
δ 2.20–2.60 ppm. The ^{13}C NMR spectra further support the structure with distinct chemical shifts corresponding to the carbonyl (δ 164–199 ppm), aromatic carbons (δ 120–160 ppm), and methyl groups (δ 14–40 ppm). The CHN analysis confirms the elemental composition, showing close agreement with the calculated values for carbon, hydrogen, and nitrogen content, which supports the molecular formulas and structural assignments.

A reasonable mechanism for forming **7a–g** from derivative **5** is illustrated in Scheme 2. Wherein the hydrazonil chlorides **6a–g** react with a di-thioester derivative **5** (thiol form, $-\text{SH}$) to yield the hydrazonic thioanhydride (i), it undergoes intermolecular cyclization to form intermediate (iii), or through 1,3-dipolar cycloaddition of nitrileimine (ii) [prepared from the hydrazonil chlorides **6a–g** *in situ* under basic conditions (triethylamine)], to

the activated double bond (thiocarbonyl group ($\text{C}=\text{S}$)) of di-thioester derivative **5**, which then cyclizes, followed by losing methyl thiol (CH_3SH), from cycloadduct (iii) to give **7a–g**. The constitution of compounds **7a–g** was verified through analytical and spectroscopic data and synthesis approaches.

2.2. *In vitro* evaluations

2.2.1. Cytotoxicity. The cytotoxic activity of the synthesized nicotinamide–thiadiazol hybrids was evaluated against two human breast cancer cell lines (MDA-MB-231 and MCF-7) and two normal cell lines (WI-38 and WISH) to assess selectivity. The results indicate that several derivatives exhibited promising anticancer activity, with some compounds displaying IC_{50} values comparable to or better than sorafenib (SOR), a well-established VEGFR-2 inhibitor.



Scheme 1 The synthetic methodology exploited for the synthesis of nicotinamide derivatives 7a–g.

Among the tested compounds, **7a** ($IC_{50} = 4.64 \pm 0.3 \mu M$ in MDA-MB-231 and $7.09 \pm 0.5 \mu M$ in MCF-7) exhibited the most potent cytotoxicity, surpassing the activity of SOR ($IC_{50} = 7.61 \pm 0.4 \mu M$ in MDA-MB-231 and $7.29 \pm 0.3 \mu M$ in MCF-7). More importantly, **7a** demonstrated a very weak cytotoxicity against WI-38 and WISH normal cell lines ($IC_{50} = 73.58 \pm 3.8 \mu M$ and $57.70 \pm 3.3 \mu M$, respectively), indicating a high degree of safety.

Additionally, compounds **7c** ($IC_{50} = 13.83 \pm 1.2 \mu M$ in MDA-MB-231, $20.52 \pm 1.4 \mu M$ in MCF-7) and **7e** ($IC_{50} = 7.90 \pm 0.6 \mu M$ in MDA-MB-231, $10.37 \pm 0.8 \mu M$ in MCF-7) also demonstrated notable anticancer activity, with **7e** exhibiting a cytotoxic profile similar to sorafenib. The lower IC_{50} values of these compounds suggest effective inhibition of VEGFR-2-mediated tumor growth and angiogenesis.

Conversely, compounds **7f** and **7g** displayed higher IC_{50} values ($>47 \mu M$ in both cancer cell lines), indicating weaker cytotoxic effects. Similarly, **7d** and **7b** exhibited moderate activity, with IC_{50} values ranging between 22 and $36 \mu M$, suggesting that structural modifications could enhance their potency.

The selectivity index (SI) is a critical parameter in evaluating the therapeutic potential of anticancer agents, as it reflects the ability of a compound to target cancer cells while minimizing toxicity to normal cells. As shown in Table 1, **7a** exhibited significantly higher SI values compared to sorafenib, with SI = 15.86 for MDA-MB-231 and SI = 8.14 for MCF-7, whereas sorafenib demonstrated much lower selectivity (SI = 1.40 and 1.84, respectively). These results suggest that **7a** possesses a strong preference for cancer cells over normal cells, indicating a potentially safer profile with reduced off-target cytotoxicity.

2.2.2. Structure–activity relationship (SAR). The cytotoxic activity of compounds **7a–7g** was evaluated against MDA-MB-

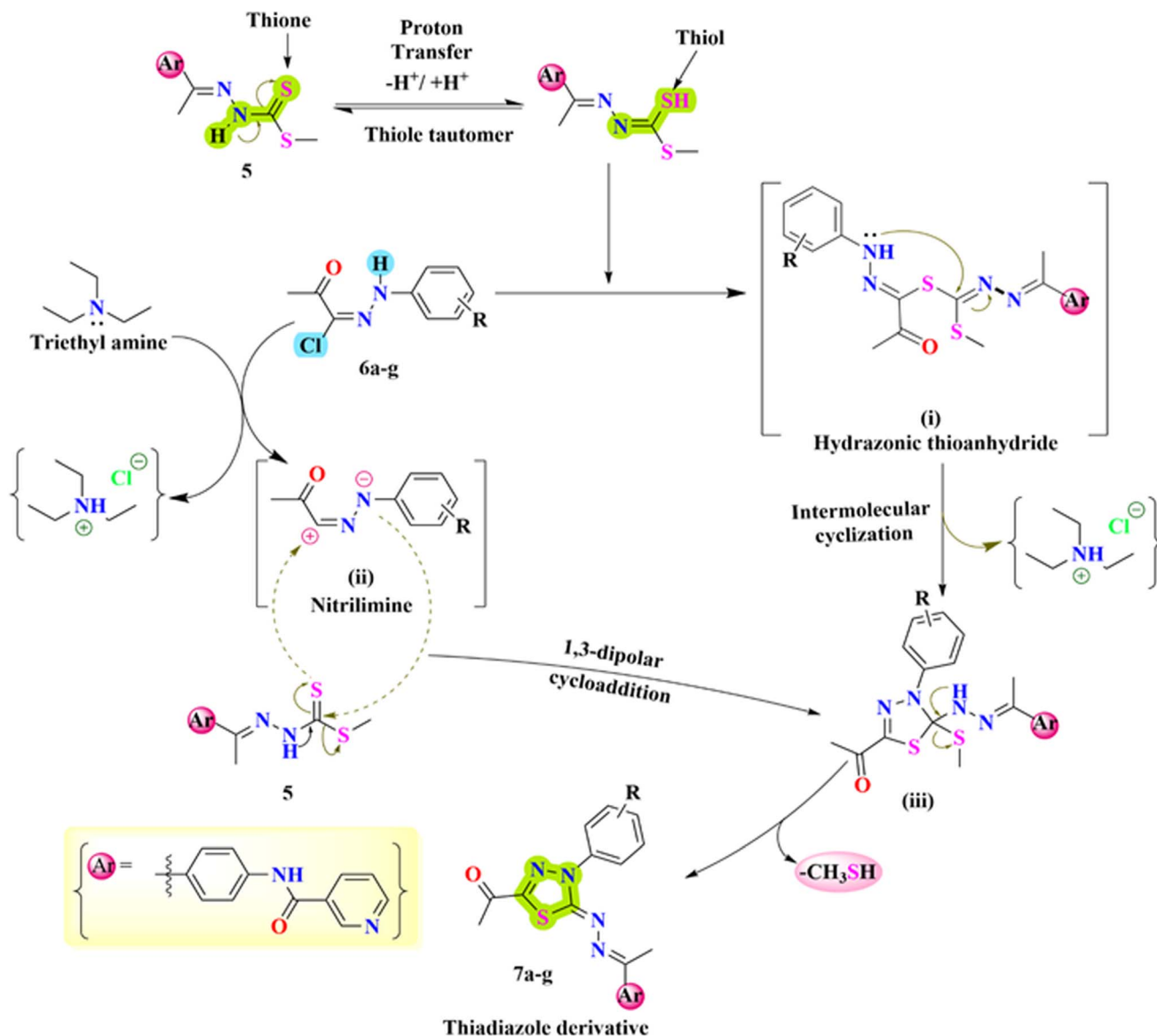
231 and MCF-7 cell lines. Sorafenib was used as the reference drug. Lower IC_{50} values indicate higher potency (Fig. 2).

2.2.2.1. Effect of hydrophobic versus hydrophilic substituents. Hydrophobic substituents generally improve cytotoxic activity, while hydrophilic groups tend to reduce it. For example, compound **7b** (IC_{50} : $22.68 \mu M$ for MDA-MB-231, $36.78 \mu M$ for MCF-7), which contains a hydrophobic 4-Cl group, exhibited significantly better activity than compound **7f** (IC_{50} : $47.74 \mu M$ for MDA-MB-231, $58.25 \mu M$ for MCF-7), which has a hydrophilic 4-NO₂ group. This suggests that increased hydrophobicity enhances the interaction with the biological target.

Interestingly, compound **7e** (IC_{50} : $7.90 \mu M$ for MDA-MB-231, $10.37 \mu M$ for MCF-7), which contains both a hydrophobic (4-Cl) and a hydrophilic (6-NO₂) group, demonstrated greater cytotoxic activity than compound **7b** (IC_{50} : $22.68 \mu M$ for MDA-MB-231, $36.78 \mu M$ for MCF-7), which has only the hydrophobic 4-Cl group. This indicates that a balanced hydrophobic–hydrophilic environment can enhance activity, possibly by improving bioavailability or target binding.

2.2.2.2. Effect of mono- versus di-substitution. Mono-substituted compounds showed superior activity compared to di-substituted compounds. Compound **7c** (IC_{50} : $13.83 \mu M$ for MDA-MB-231, $20.52 \mu M$ for MCF-7) and compound **7d** (IC_{50} : $31.77 \mu M$ for MDA-MB-231, $28.81 \mu M$ for MCF-7), which feature single methyl groups at the 3- and 4-positions, respectively, exhibited significantly stronger activity than compound **7g** (IC_{50} : $60.53 \mu M$ for MDA-MB-231, $49.51 \mu M$ for MCF-7), which contains two methyl groups at the 3- and 4-positions. This suggests that di-substitution at adjacent positions (3,4-di-CH₃) may introduce steric hindrance, reducing the binding efficiency and lowering the overall cytotoxic effect.





Scheme 2 Anticipated mechanism for the synthesis of the target nicotinamide derivatives 7a–g.

Table 1 *In vitro* cytotoxicity (IC₅₀) of synthesized nicotinamide–thiadiazol hybrids against breast cancer and normal cell lines

Comp.	<i>In vitro</i> cytotoxicity IC ₅₀ ^a (μM)			
	MDA-231	MCF-7	WI-38	WISH
7a	4.64 ± 0.3	7.09 ± 0.5	73.58 ± 3.8	57.70 ± 3.3
7b	22.68 ± 1.5	36.78 ± 2.2	—	—
7c	13.83 ± 1.2	20.52 ± 1.4	—	—
7d	31.77 ± 2.1	28.81 ± 1.9	—	—
7e	7.90 ± 0.6	10.37 ± 0.8	—	—
7f	47.74 ± 2.7	58.25 ± 3.3	—	—
7g	60.53 ± 3.4	49.51 ± 2.8	—	—
SOR	7.61 ± 0.4	7.29 ± 0.3	10.64 ± 0.8	13.44 ± 1.1

^a The values are expressed as the mean ± SEM from three independent experiments.

2.2.2.3. Effect of substituent position (*meta* versus *para*). The position of the substituent also influences activity. *Meta*-substitution, as seen in compound 7c (IC₅₀: 13.83 μM for MDA-MB-231, 20.52 μM for MCF-7), resulted in better cytotoxicity than *para*-substitution, as in compound 7d (IC₅₀: 31.77 μM for MDA-MB-231, 28.81 μM for MCF-7). This suggests that *meta*-positioning may enhance receptor binding, possibly due to steric or electronic interactions.

2.2.2.4. Effect of *ortho* versus *para* substitution. *Ortho*-substitution proved to be significantly more beneficial than *para*-substitution. Compound 7a (IC₅₀: 4.64 μM for MDA-MB-231, 7.09 μM for MCF-7), which contains a 2-Cl (*ortho*) substituent, exhibited much stronger activity than compound 7b (IC₅₀: 22.68 μM for MDA-MB-231, 36.78 μM for MCF-7), which has a 4-Cl (*para*) substituent. This indicates that placing chloro atom at

Hydrophobic (4-Cl of comp. 7b) > Hydrophilic (4-NO₂ of comp. 7f)
 Hydrophobic & Hydrophilic (4-Cl-6-NO₂ of comp. 7e) > Hydrophilic (4-Cl of comp. 7b)
 Mono-substitution (3-CH₃ & 4-CH₃ of comp. 7c & 7d) > Disubstitution (3,4-di-CH₃ of comp. 7g)
 Meta-substitution (3-CH₃ of comp. 7c) > Para-substitution (4-CH₃ of comp. 7d)
 Ortho-substitution (2-Cl of comp. 7a) > Para-substitution (4-Cl of comp. 7b)

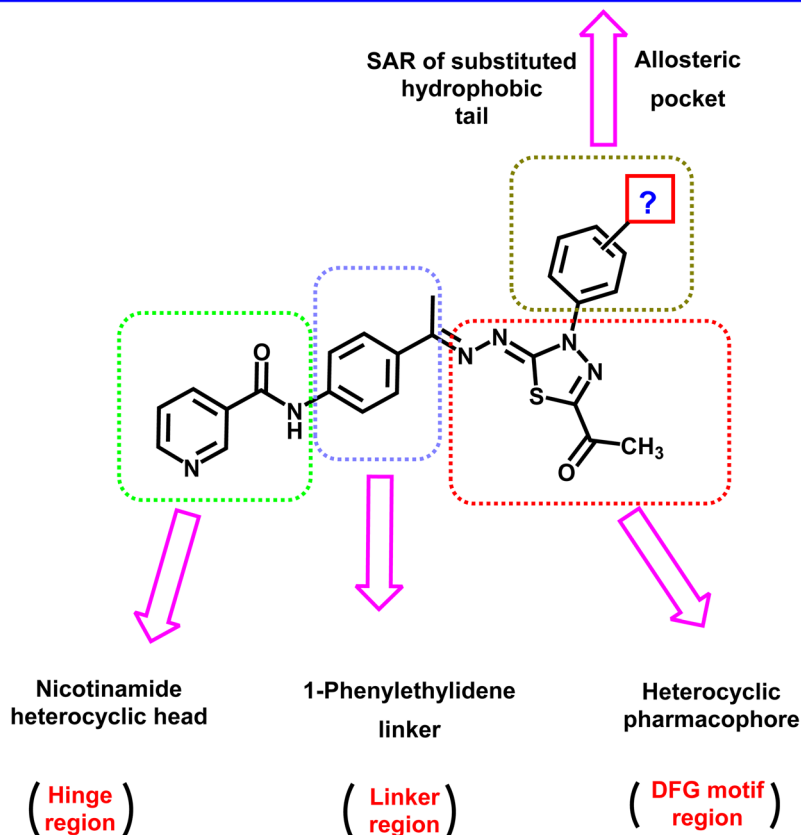


Fig. 2 Structure–activity relationship (SAR) of the synthesized compounds based on the cytotoxic evaluation against MDA-MB-231 and MCF-7 cell lines.

the *ortho* position enhances interactions with the biological target, leading to increased potency.

2.2.3. *In vitro* VEGFR-2 assay. The cytotoxic evaluation of the synthesized nicotinamide–thiadiazol hybrids demonstrated their potential as promising anticancer activity. Notably, **7a** exhibited the most potent cytotoxicity among the tested compounds. Further enzymatic inhibition assays confirmed that **7a** effectively inhibits VEGFR-2, with an IC₅₀ value of 0.095 ± 0.05 μM, comparable to sorafenib (0.1 ± 0.05 μM). This suggests that **7a** directly targets VEGFR-2 with high potency, supporting its role as a promising anti-angiogenic agent.

The strong VEGFR-2 inhibition observed for **7a** likely contributes to its ability to suppress angiogenesis and tumor

progression. This result aligns with its potent cytotoxic effects against cancer cells, reinforcing our design.

2.2.4. MDA-MB-231 cell cycle analysis. To further understand the mechanism of action of **7a**, cell cycle analysis on MDA-MB-231 cells was performed. The results (Table 2 and Fig. 3) reveal a significant alteration in cell cycle distribution following treatment with **7a**, indicating its potential role in cell cycle arrest. In untreated control cells, the distribution of cells across the phases was 12% in G₀/G₁, 45% in S, and 43% in G₂/M. However, treatment with **7a** led to a remarkable shift, with 33% of cells in G₀/G₁, 59% in S, and only 8% in G₂/M, suggesting an S-phase arrest and impairing the progression to the G₂/M phase. The corresponding decrease in the G₂/M phase fraction (from 42.77% to 8%) suggests that **7a** effectively prevents cells from entering mitosis, leading to potential apoptotic signalling. This pattern is consistent with other VEGFR-2 inhibitors that induce S-phase arrest by disrupting VEGF-mediated survival pathways.

2.2.5. Apoptosis and necrosis rates of MDA-MB-231. To further evaluate the anticancer effects of **7a**, apoptosis analysis

Table 2 The impact of compound **7a** on MDA-MB-231 cell cycle

Sample	G0/G1	S	G2/M
Control MDA-MB-231	12%	45%	43%
Comp. 7a/MDA-MB-231	33%	59%	8%



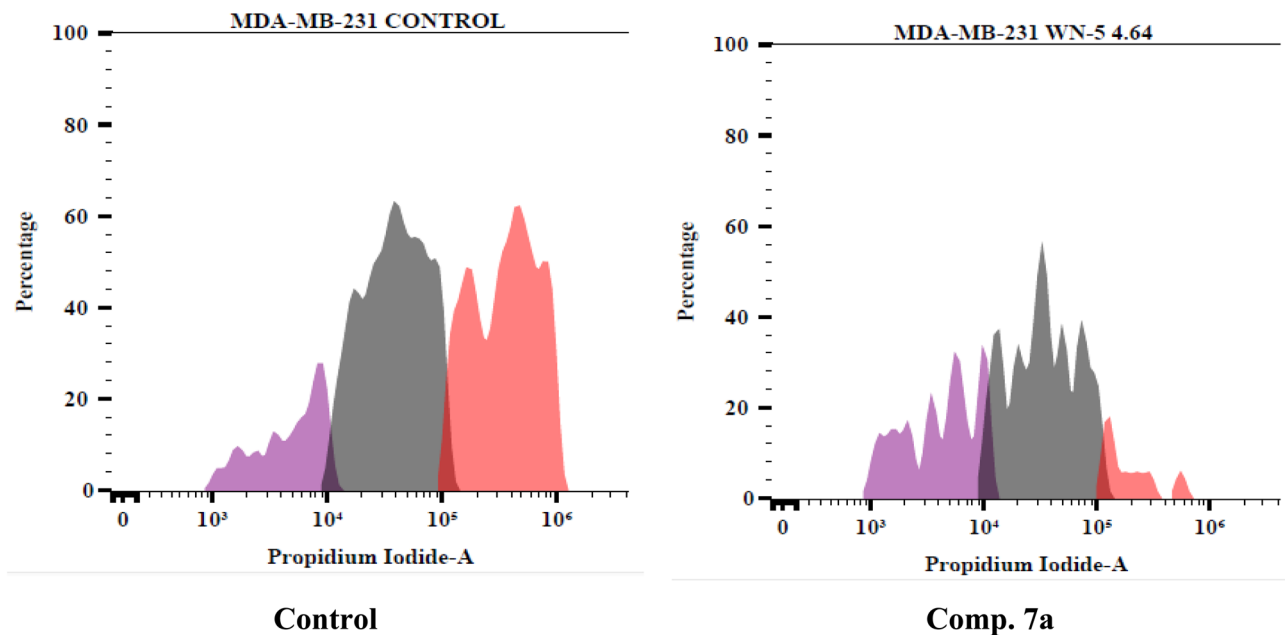


Fig. 3 The effect of comp. 7a on different phases of MDA-MB-231 cell cycle.

Table 3 Effect of compound 7a on apoptosis and necrosis rates of MDA-MB-231 cells

Sample	Viable cells	Early apoptosis	Late apoptosis	Necrosis
Control	99.30%	0.48%	0.03%	0.19%
Comp. 7a	49.99%	1.06%	44.01%	4.94%

was conducted to assess its impact on cell viability and programmed cell death in MDA-MB-231 cells. The results (Table 3 and Fig. 4) demonstrate a significant shift from viable cells to

apoptotic and necrotic populations following treatment with 7a, indicating its strong pro-apoptotic activity.

In the untreated control group, 99.30% of the cells remained viable, with minimal signs of apoptosis (0.48% early apoptosis, 0.03% late apoptosis) or necrosis (0.19%). However, treatment with 7a drastically reduced cell viability to 49.99%, while markedly increasing late apoptosis (44.01%) and necrosis (4.94%). The minimal increase in early apoptosis (1.06%) suggests that 7a induces rapid apoptotic progression, leading to a higher proportion of cells in the late apoptotic stage.

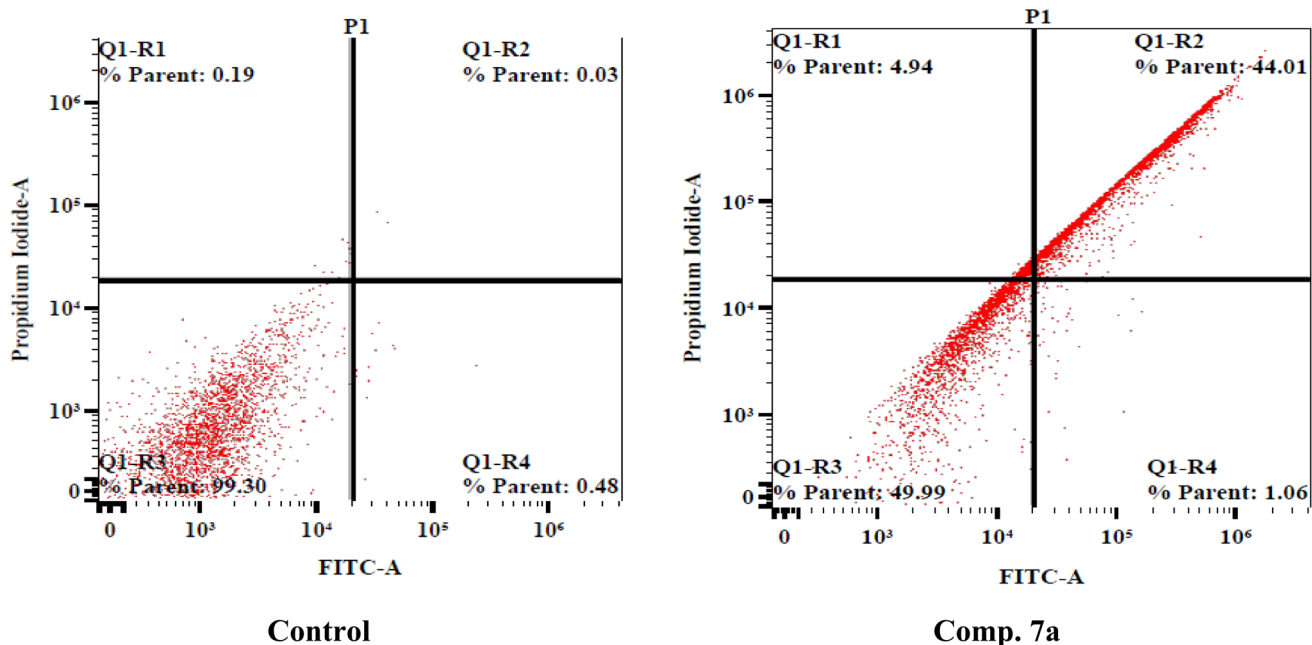


Fig. 4 Apoptosis and necrosis rates of MDA-MB-231 cells treated with compound 7a compared to control.

Table 4 Modulation of apoptosis-related genes (caspase-3, Bcl-2, Bax) by compound **7a** in MDA-MB-231 cells

Code	Caspase-3 conc.	FLD	Bcl-2 conc.	FLD	Bax conc.	FLD
Comp. 7a	441.93	8.2	1.53	3.68	394.72	6.9
Cont. MDA-MB-231	53.61	1	5.64	1	56.9	1

The substantial rise in late apoptosis indicates that **7a** effectively triggers cell death pathways, possibly through VEGFR-2 inhibition and downstream disruption of pro-survival signaling. The slight increase in necrotic cells suggests that a subset of cells undergoes non-apoptotic death, which may be due to high-dose cytotoxic effects or secondary necrosis following prolonged apoptosis.

2.2.6. Impact of compound **7a on BAX, BCL-2 and caspase-3 pathway.** The expression levels of key apoptosis-related proteins, including caspase-3, Bcl-2, and Bax of MDA-MB-231 cells treated with compound **7a** were investigated using ELISA technique. The results demonstrate a strong activation of apoptosis following treatment with **7a**, providing molecular evidence of its pro-apoptotic effects.

As shown in Table 4, caspase-3, a key effector protease in the execution phase of apoptosis, was significantly upregulated in **7a**-treated cells (441.93; FLD = 8.2) compared to the untreated control (53.61; FLD = 1). This substantial increase suggests that **7a** effectively activates caspase-dependent apoptotic pathways, leading to programmed cell death. Conversely, the anti-apoptotic protein Bcl-2 was markedly downregulated following **7a** treatment (1.53; FLD = 3.68) compared to control cells (5.64; FLD = 1). This decrease in Bcl-2 expression indicates suppression of survival signaling, thereby promoting apoptosis. In contrast, the pro-apoptotic protein Bax was significantly upregulated (394.72; FLD = 6.9) compared to control cells (56.9; FLD = 1), further supporting the induction of apoptosis through the mitochondrial (intrinsic) pathway. The observed Bax upregulation, Bcl-2 downregulation, and caspase-3 activation collectively suggest that **7a** triggers apoptosis through intrinsic mitochondrial signaling.

2.3. *In silico* evaluations

2.3.1. Molecular docking study. A molecular docking analysis was undertaken to validate the binding affinity of the most active nicotinamide-thiadiazol hybrid **7a** to its biomolecular targets, VEGFR-2, based on the previously obtained

biological data. The study was conducted using sorafenib as a reference inhibitor.

Validation of the docking protocol was first carried out by re-docking the co-crystallized sorafenib (PDB ID 4ASD) into its specific binding site. The docked conformation was compared to its native conformation, resulting in a notably low RMSD value (RMSD = 1.15 Å) as shown in Fig. 5. This result confirmed the reliability of the docking approach and validated the correctness of the binding evaluation.

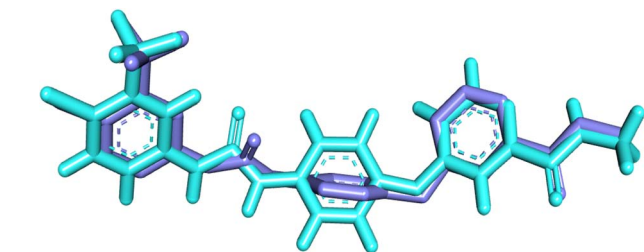
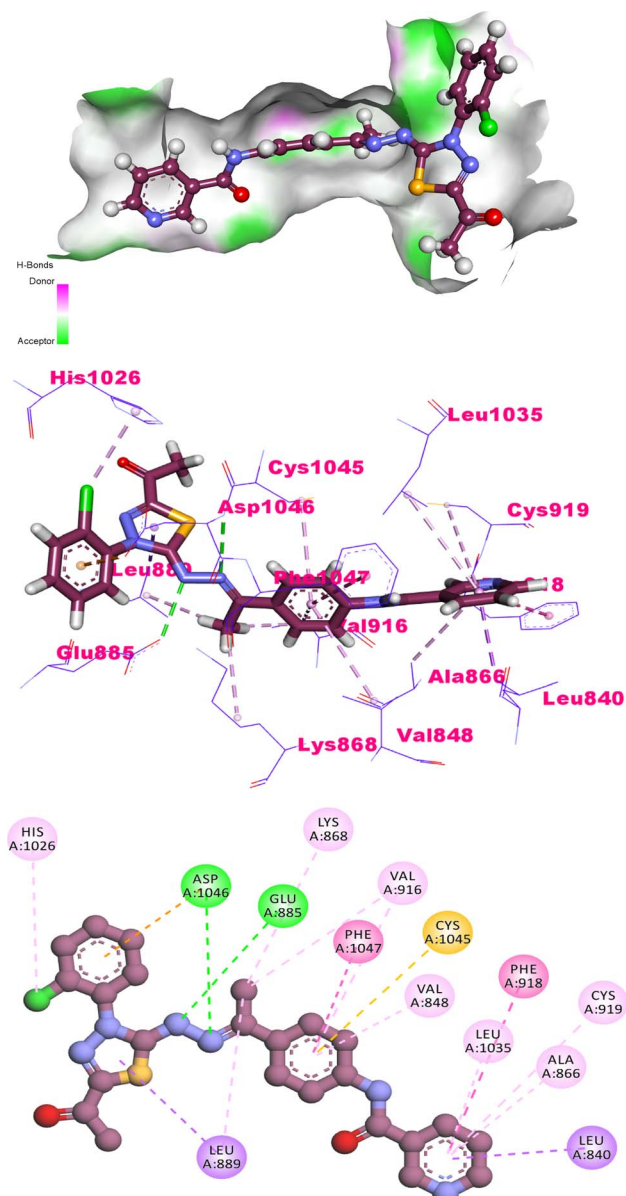


Fig. 5 Validation within VEGFR-2 active pocket through the superimposition of the docked ligand (purple) upon the original ligand (turquoise).

Fig. 6 MS, 3D, and 2D images of the most promising nicotinamide derivative **7a** interacted with the VEGFR-2 active site.



The docking of a reference inhibitor (sorafenib) demonstrated binding interactions with Cys917, Asp1044, and Glu883, which are key residues in the active pocket, as illustrated in

Fig. S2.† The main four areas of the VEGFR-2 pocket were likewise shown to be occupied by compound **7a**. Compound **7a**'s nicotinamide moiety formed several hydrophobic

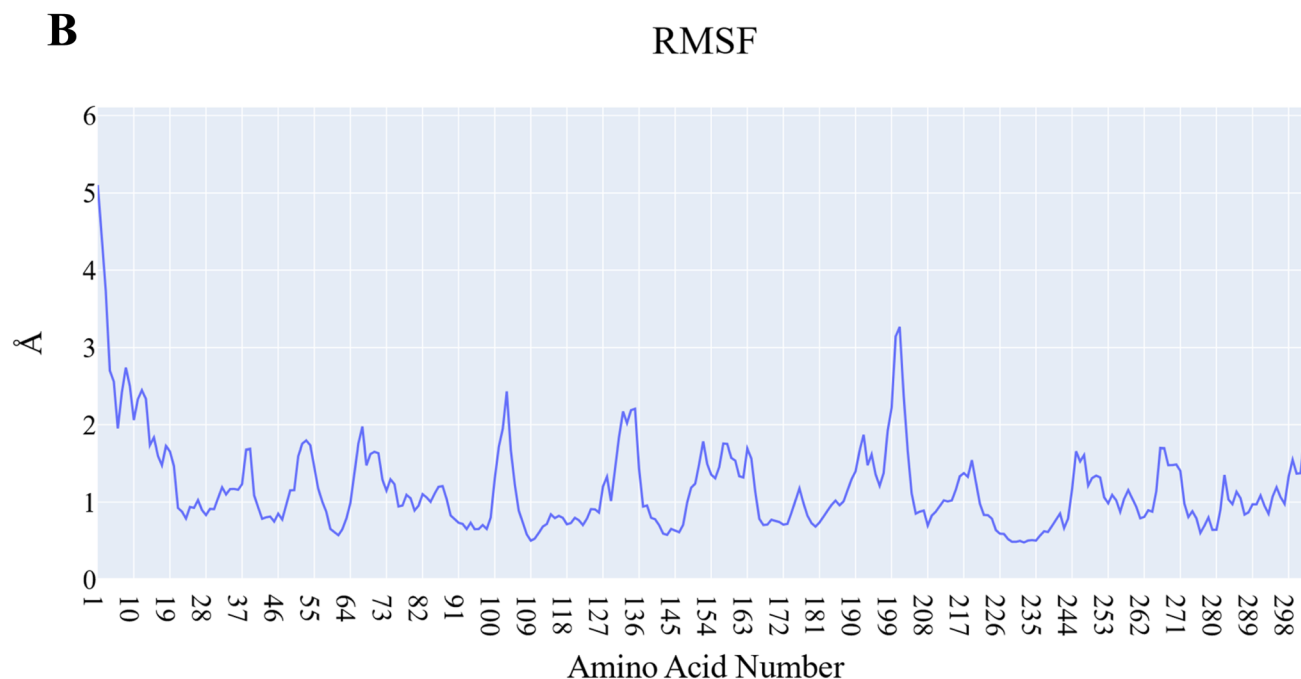
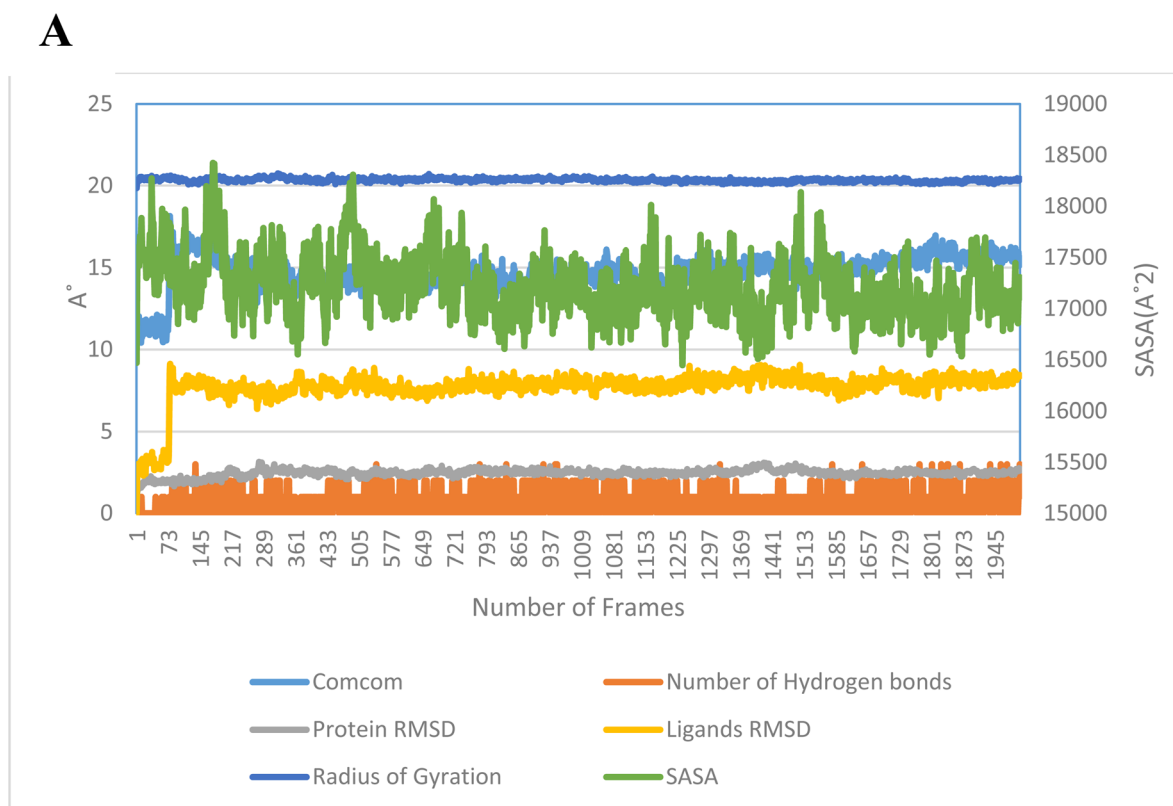


Fig. 7 (A) RMSD values from the trajectory for the VEGFR-2, **7a** RMSD values, RoG for the VEGFR-2 protein in the VEGFR-2_7a complex, SASA for the VEGFR-2 protein in the VEGFR-2_7a complex, change in the number of hydrogen bonds and distance from the center of mass of **7a** compound and VEGFR-2 protein. (B) RMSF for the VEGFR-2 protein in VEGFR-2_7a complex.



interactions, including an important one with Cys917, inside the hinge area. Additionally, two pi-pi interactions were accomplished by the central phenyl (spacer) moiety with Val916 and Val848. An additional two crucial hydrogen bonds were formed in the inner DFG-motif region by compound **7a** using its ethylenedihydrazine moiety with Asp1046 and Glu885. Furthermore, the hydrophobic region's amino acids reacted with the active candidate's 2-acetyl-4-phenyl-4,5-dihydro-1,3,4-thiadiazol group (Fig. 6).

2.3.2. MD simulations. Different dynamics of VEGFR-2 upon binding **7a** were observed using MD simulations. The VEGFR-2 backbone in the VEGFR-2_7a complex (Fig. 7A) maintained stable RMSD values around 2.5 Å throughout the simulation, indicating minimal conformational fluctuations. The ligand RMSD profile (Fig. 7B) displayed stable values around 8 Å at 10 ns to the end of the simulation. Before this point in time, the RMSD value gradually rises until reaching 8 Å.

Average RoG and SASA values (Fig. 7C and D) indicate no significant changes in the overall structure of the protein. Hydrogen bond analysis (Fig. 7E) revealed that the complex formed a relatively constant two hydrogen bonds throughout the simulation, with a small number of frames showing three H-bonds. RMSF profiles of C-alpha atoms (Fig. 7F) showed minimal fluctuations for the system around (1.5–2.5 Å). The center-of-mass distance analysis (Fig. 7G) indicated stable ligand binding after 10 ns, around the average distance of 14 Å, but before this period, the stabilizing average distance was increasing around (12–18 Å). Overall, these findings suggest that the complex remains stable during the simulation.

2.3.3. MMGBSA evaluations. Fig. 8 unveils the intricate components of the predicted binding free energies of VEGFR-2_7a complex calculated using the MM-GBSA method. The total binding affinity of the complex ($-28.99 \text{ kcal mol}^{-1}$) and the robust van der Waals interactions averaging around

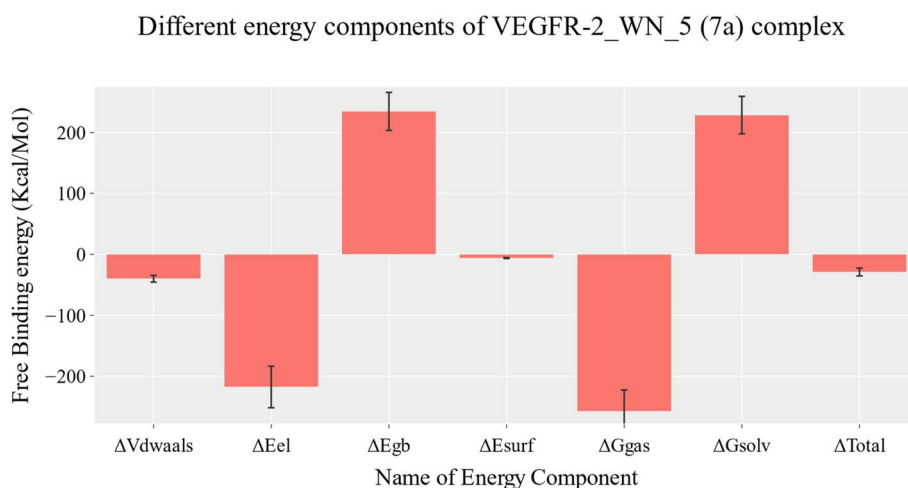


Fig. 8 Energetic components and their values for the VEGFR-2_7a complex.

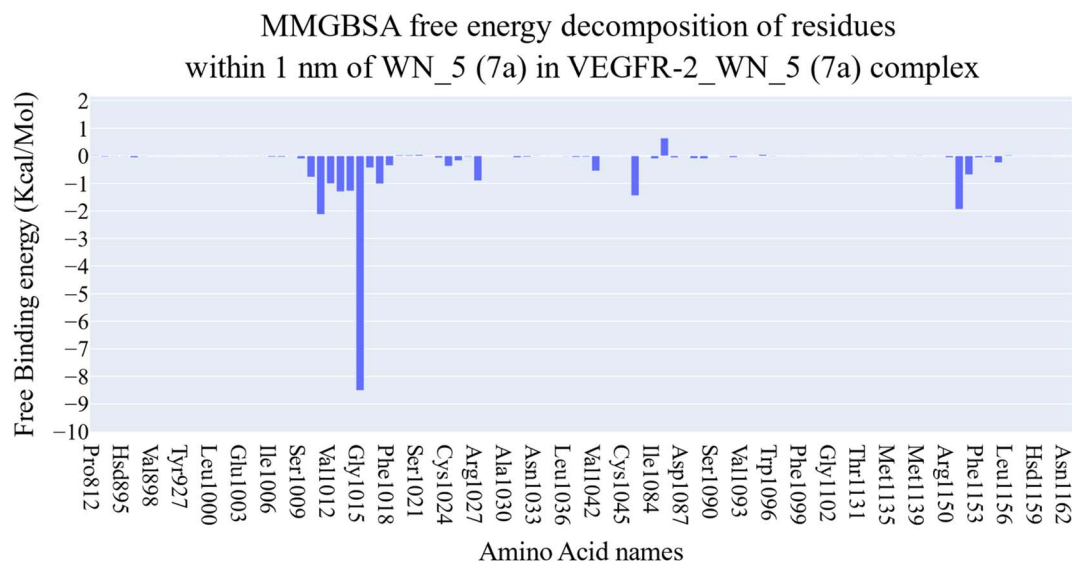


Fig. 9 Binding free energy decomposition of the VEGFR-2_7a complex.



−40.04 kcal mol^{−1} and the electrostatic contributions (−217.6 kcal mol^{−1}). To pinpoint the contribution of amino acid residues within 1 nm of each ligand, decomposition analysis was performed (Fig. 9). Interestingly, there are more than ten residues that exhibit enhanced contributions to **7a** binding. Such as of these amino acids are PHE1010 (−0.76 kcal mol^{−1}), GLN1011 (−2.13 kcal mol^{−1}), VAL1012 (−1 kcal mol^{−1}), ALA1013 (−1.29 kcal mol^{−1}), LYS1014 (−1.27 kcal mol^{−1}), GLY1015 (−8.5 kcal mol^{−1}), GLU1017 (−1.011 kcal mol^{−1}), ARG1027 (−0.9 kcal mol^{−1}), ARG1027 (−0.9 kcal mol^{−1}), TRP1071 (−1.44 kcal mol^{−1}), PRO1151 (−1.94 kcal mol^{−1}) and positive contribution GLN1085 (+0.65 kcal mol^{−1}).

2.3.4. Protein–ligand interaction fingerprints (ProLIF) analysis. ProLIF analysis provided valuable insights into the specific amino acids involved in ligand interactions within the VEGFR-2 binding pocket, highlighting the molecular details that govern the binding affinity and specificity of the ligands. Fig. 10 illustrates one particularly important amino acid, ASP807, which demonstrated a high propensity for anionic interaction, occurring in more than 80% of the analyzed ligand-binding frames (83% occurrence). This indicates that ASP807 plays a crucial role in stabilizing the ligand through electrostatic interactions, contributing significantly to the overall

binding strength. In contrast, the other amino acids within the binding pocket were primarily involved in van der Waals (VdW) contact interactions, with each showing an occurrence frequency of less than 80%. These VdW interactions, while still contributing to ligand stabilization, are less consistent compared to the anionic interaction involving ASP807.

2.3.5. Principal component analysis of trajectories (PCAT). PCA method was chosen for identifying coordinated movements of the α -carbon atoms in the VEGFR-2_7a complex. Several factors listed in the ESI† methods section have to be carefully considered to determine the reduced subspace's proper dimensions. These included the cumulative variance explained by increasing the number of principal components (PCs), the scree plot, and the eigenvector distribution. The scree plot (Fig. 11) showed that the slope began to significantly reduce at the third PC, indicating a possible point of inflection for the selection of dimensionality. As seen in Fig. 11, the first eigenvector alone accounted for a significant 73.9% of the overall variance, while the first three PCs combined contributed roughly 82.5%. This suggested that these three PCs accounted for a sizable fraction of the total protein movements. The distributions of the first five PCs differed from the Gaussian distribution, which further supported this decision (Fig. 12). A non-Gaussian distribution frequently indicates the existence of significant, non-random motions that these components can record. We thus chose the top six PCs as examples of the crucial subspace based on a combination of the scree plot, variance collected, and non-Gaussian eigenvector distributions. We subsequently examined the cosine content of the first ten principal components (PCs) for the VEGFR-2 system (Fig. 13) to assess the randomness and possible redundancy within the identified critical subspaces. Except for the second PC (0.19 for VEGFR-2_7a complex) and the fourth PC of the complex (0.162). This suggests that the identified essential motions captured by the PCs are not random.

2.3.6. Free energy landscape (FEL) analysis. The projected trajectories onto various two-dimensional planes defined by the

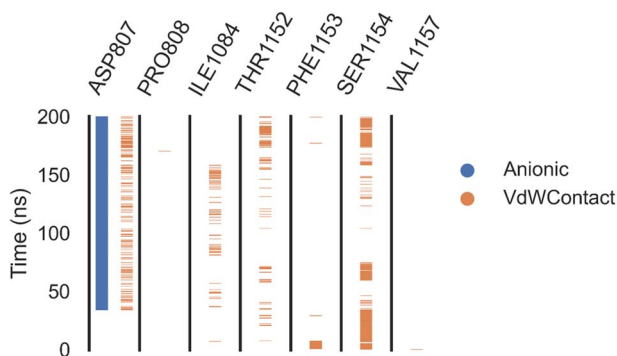


Fig. 10 Amino acids, interactions types of VEGFR-2 and 7a.

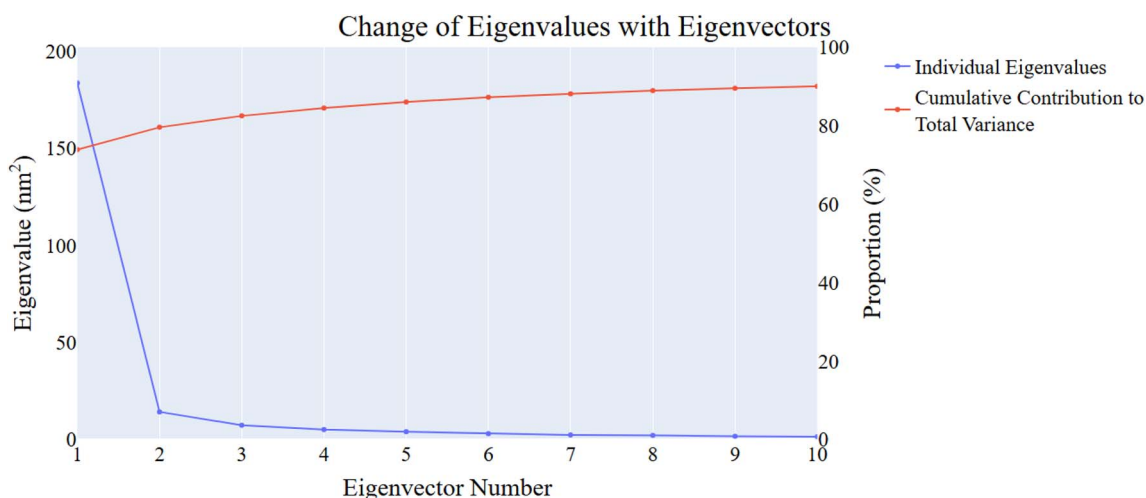


Fig. 11 Eigenvalues' changes showing an increase in eigenvectors (blue) and retained cumulative variance in the eigenvectors (red).

Histogram of the first 10 PCs

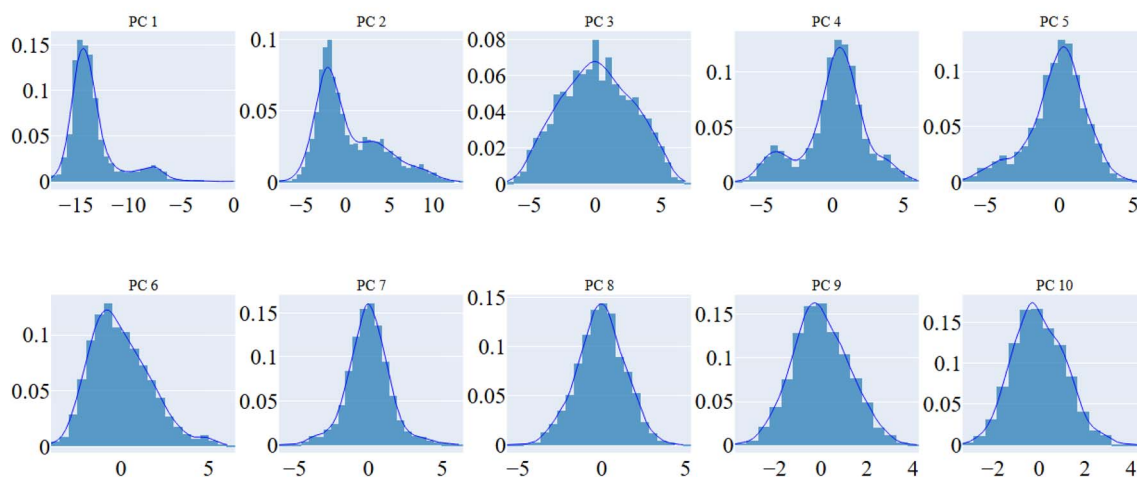


Fig. 12 The initial ten eigenvectors' distribution.

Cosine content

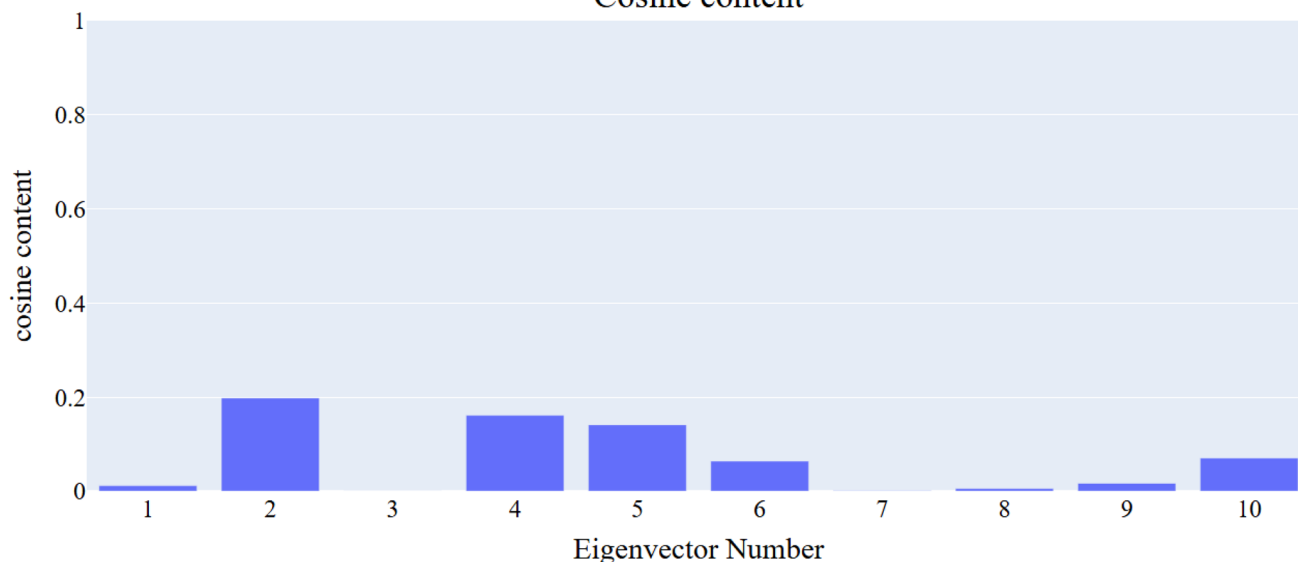


Fig. 13 Cosine content values of the initial ten eigenvectors for the trajectory.

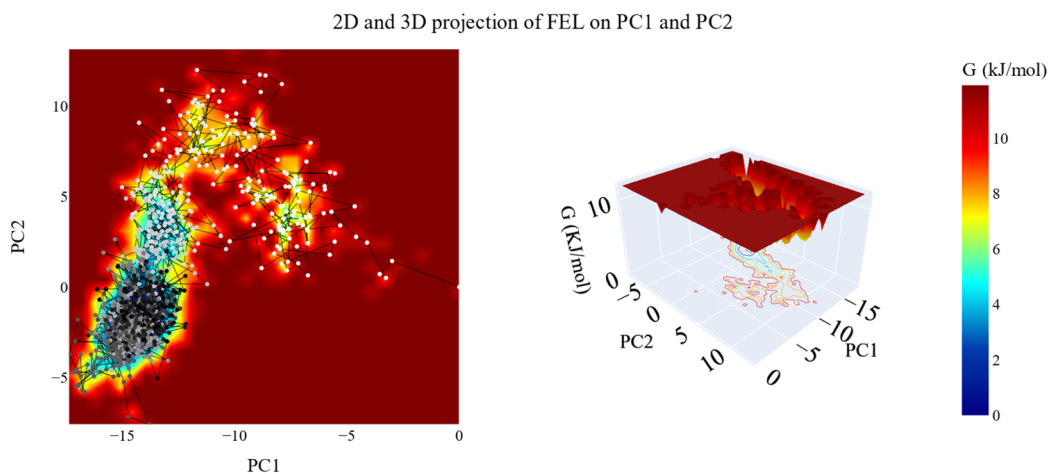
chosen PCs are displayed in Fig. 14. Every graphic displays a different landscape with different basins that correspond to local minima on the FEL. These basins correspond to preferred conformations adopted by the protein–ligand complex during the simulation. For the projection on the first two PCs (Fig. 14A), the sampling starts from (white dots) basin and then moves to a transient basin (white grey dots) before finally reaching the most stable one (dark grey and black dots). There is a 0.6 kJ mol^{-1} difference between the global minimum and the next minimum. Fig. 14B presents the PC1–PC3 projection, which shows a projection with two basins, the trajectories move from the transient basin to the stable basin. The energy difference between the global minimum and the next minimum is calculated to be 0.38 kJ mol^{-1} . Similarly, Fig. 14C demonstrates the projection on the PC2 and PC3, revealing that the trajectory

begins in the middle basin and then transitions to two different basins before eventually reaching the most stable basin at the end of the simulation (black dots). The difference between the second and global minima is $0.156 \text{ kJ mol}^{-1}$.

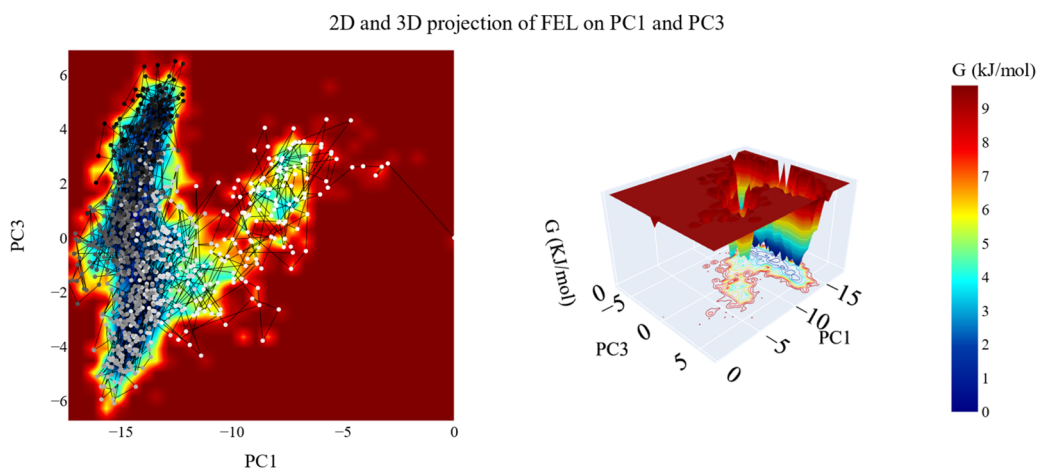
2.3.7. DFT analysis. Using the DFT/6-31+G(d,p) level of theory, the chemical system of **7a** was optimized using the Gaussian 09W computer program. GaussView 03 and Multiwfn were two complementing computer programs used for the analyses. Both the dipole moment and total ground state energy are shown in Table 5. Compound **7a** was tuned to the lowest energy before being labeled and shown in Fig. 15A. A feature that provides insight into how a chemical system will behave in its environment is the dipole moment. The compound's comparatively high dipole moment value (8.796 debye) indicates that hydrogen bonds will form, and dipole–dipole



A



B



C

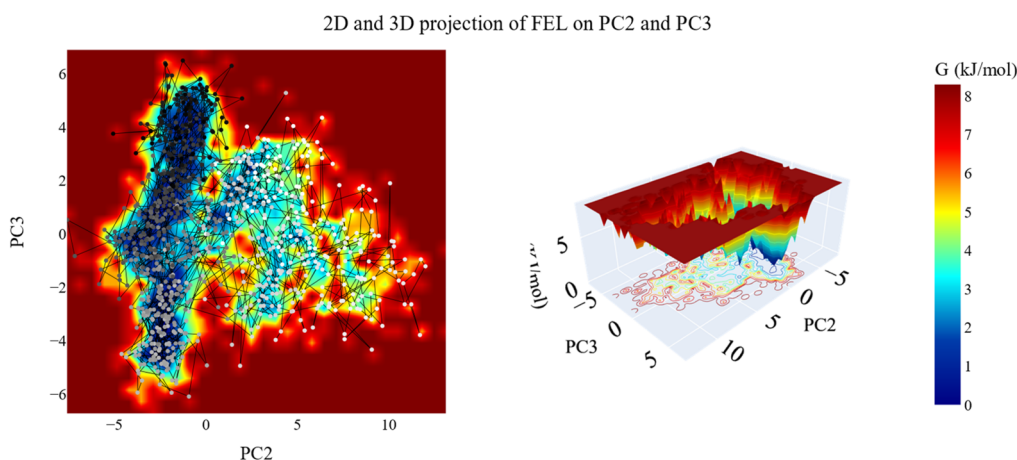


Fig. 14 2D and 3D projection of the VEGFR-2_7a trajectory's FEL on (A) first two, (B) first and third and (C) second and third eigenvectors.

interactions will be involved. Since the dipole moment indicates the polarity of the molecule, high values indicate a significant separation of charges. The chemical system is more suited to

interact with the protein target site since it is a polar molecule with a significant charge separation. Mulliken charge has been examined and shown in Fig. 15B since the charge separation

Table 5 The DFT calculated global reactivity parameters for 7a

IP	EA	μ (eV)	χ (eV)	η (eV)	σ (eV)	ω (eV)	D_m (debye)	TE (eV)	ΔN_{\max}	ΔE (eV)
5.846	2.531	-4.189	4.189	1.658	0.603	14.542	8.796	-61 589.613	2.527	-14.542

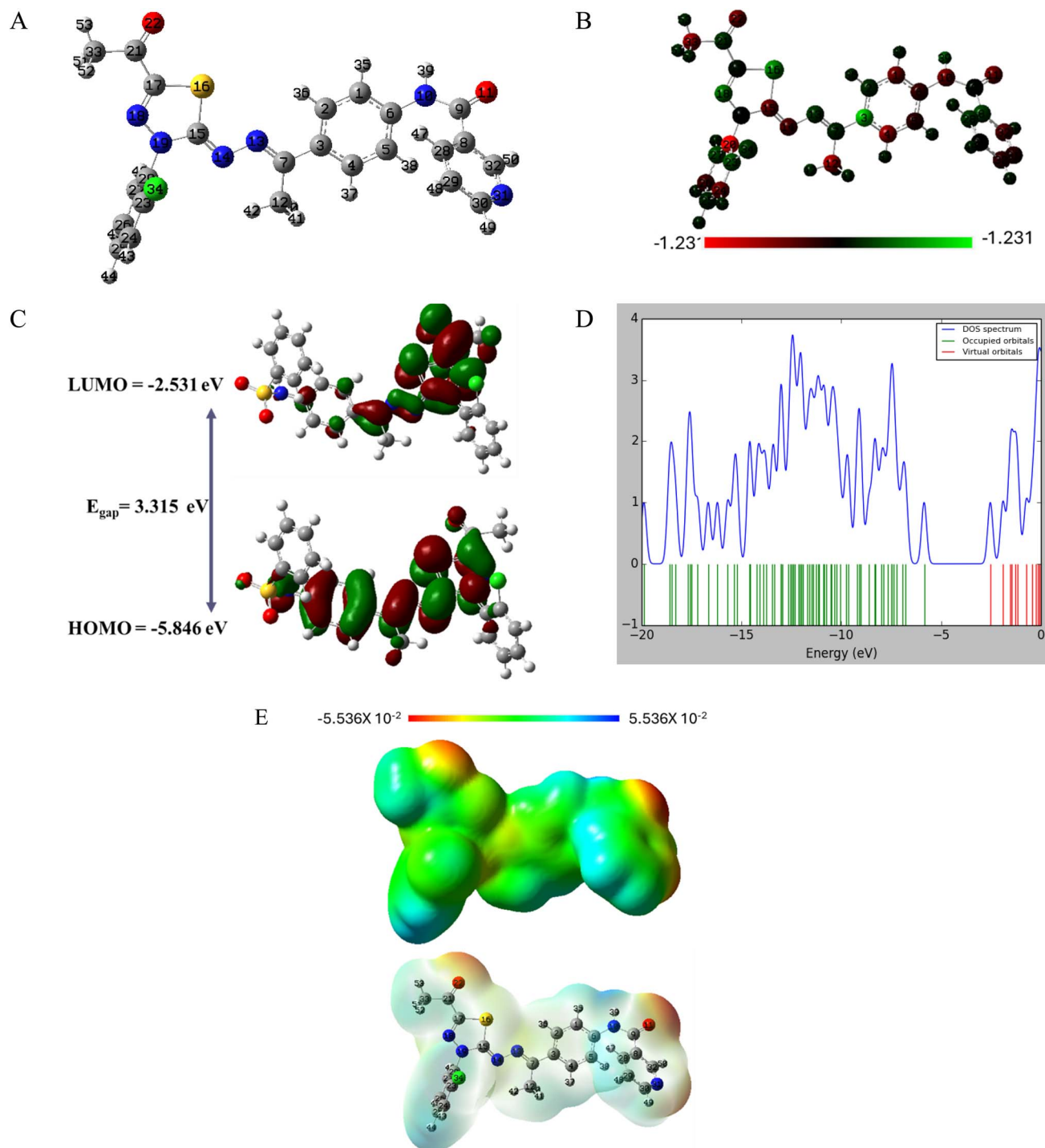


Fig. 15 The optimized structure (A), the Mulliken charge distribution color scale (B), the HOMO/LUMO distribution functions and energy gap (C), the TDOS analysis (D), and the molecular electrostatic potential map (E) at B3LYP/6-31G(d,p) level for 7a.

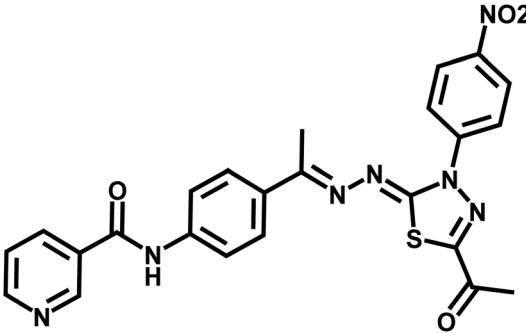
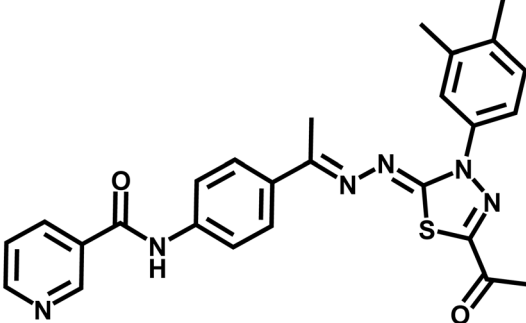
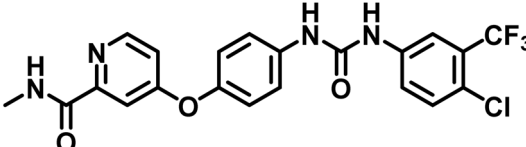


Table 6 Predicted ADMET properties of the nicotinamide–thiadiazol hybrids and sorafenib

Comp.	Structure	BBB level	Solubility level	Absorption level	CYP2D6 prediction	PPB prediction
7a						
7b						
7c		Very low	Low	Good	Non inhibitor	More than 90%
7d						
7e				Poor		



Table 6 (Contd.)

Comp.	Structure	BBB level	Solubility level	Absorption level	CYP2D6 prediction	PPB prediction
7f						Less than 90%
7g				Moderate		More than 90%
Sorafenib			Very low	Good		

influences the binding affinity towards the target. 7a exhibits a notable charge separation at multiple locations, with C3 being the most electron-rich site, as seen by the color scale in Fig. 15B. C20 is the spot with the greatest electron deficit among the molecule's atoms. Electrostatic interactions or hydrogen bonding may involve both positive and negative sites of 7a.

As demonstrated in Fig. 15A, the two terminal benzene rings are almost perpendicular to the rest of compounds which affect the lobes of HOMO and LUMO density function as shown in Fig. 15C. The two terminal benzene rings are slanted to the remaining compounds, influencing the HOMO and LUMO density function lobes. Table 5 calculates the energy gap, E_{gap} , between the border orbitals, HOMO and LUMO, as well as all related HOMO/LUMO characteristics. To understand the reactivity and possible anticancer activity, the energy gap is an essential quantity.^{39–42} 7a's band gap is relatively low ($E_{\text{gap}} = 3.315$ eV) which points to a reactive medication. The 7a, and the protein target interact as a result of the electron transport between HOMO and LUMO being facilitated by a reduced E_{gap} value. Fig. 15D shows the energy gap and total electron density surrounding HOMO/LUMO orbitals. Electronic densities increase under HOMO orbitals, indicating the drug's capacity to

give electrons. Compound 7a is soft and reactive, according to the reactivity values in Table 5.

Drug–target interactions and selectivity are shown by 7a's electrostatic surface potential, shown in Fig. 15E. The red-colored, electron-rich sites that are targeted at the oxygen atoms would be the target of the electrophilic attack, as shown in Fig. 15E. The sites appear in blue, have positive potential values. These positive sites are found over hydrogen atoms and are electron deficient. Hydrogen bonding with the protein target may involve both positive and negative potential sites. Hydrophobic interactions can occur in the green zones over conjugated systems.

2.3.8. In silico ADMET analysis. To evaluate the drug-likeness and pharmacokinetic potential of the synthesized nicotinamide–thiadiazole hybrids, key ADMET parameters—such as blood–brain barrier (BBB) permeability, aqueous solubility, intestinal absorption, CYP2D6 inhibition potential, and plasma protein binding (PPB)—were predicted using the ADMET module of Discovery Studio software.⁴³ These evaluations were conducted entirely through computational modeling; no biological samples or experimental assays were used in this study.



As Table 6 shows, all tested compounds, including **7a**, exhibited very low BBB permeability, indicating minimal central nervous system penetration. This is a favorable property for anticancer drugs, as it reduces the risk of off-target CNS toxicity. However, their low solubility levels suggest potential limitations in bioavailability, which may require formulation strategies such as nanoparticle encapsulation or prodrug modifications to enhance solubility and systemic circulation.

In terms of intestinal absorption, most compounds, including **7a**, showed good absorption, except **7e** and **7f**, which demonstrated poor absorption. This suggests that **7a** has a favorable absorption profile, similar to sorafenib, making it a viable candidate for oral administration.

Regarding metabolic stability, all compounds were classified as non-inhibitors of CYP2D6, indicating a lower risk of drug–drug interactions through this metabolic pathway. Additionally, **7a** displayed high plasma protein binding (PPB > 90%), similar to sorafenib, which may contribute to a longer half-life in systemic circulation but could also impact free drug availability for therapeutic action.

Overall, **7a** demonstrates promising pharmacokinetic properties, particularly in terms of absorption and metabolic stability, while its low solubility presents a potential challenge for bioavailability. Future studies should focus on improving its formulation for better solubility and evaluating its *in vivo* pharmacokinetics to confirm these predictions.

2.3.9. In silico toxicity analysis. The safety and potential toxicity of the synthesized nicotinamide–thiadiazol hybrids, were analyzed computationally. Their mutagenicity, carcinogenicity, toxicity classification, rat oral LD₅₀, rat chronic LOAEL, and irritation potential were investigated using Discovery

Studio software.⁴⁴ The results provide a comprehensive overview of their predicted toxicological profiles compared to sorafenib.

As Table 7 shows, all tested compounds, including **7a**, were classified as non-mutagenic except for **7f**, which was identified as a potential mutagen. Additionally, **7a** was predicted to be a non-carcinogen, while sorafenib was classified as a single carcinogen, highlighting the improved safety profile of **7a** compared to the standard VEGFR-2 inhibitor.

Regarding acute toxicity, **7a** exhibited an oral LD₅₀ value of 0.531 mg kg^{−1}, suggesting a relatively low toxicity level compared to sorafenib (0.822 mg kg^{−1}). Similarly, the rat chronic lowest observed adverse effect level (LOAEL) for **7a** (0.0618 mg kg^{−1}) was higher than that of sorafenib (0.0048 mg kg^{−1}), indicating lower chronic toxicity risk. Skin and ocular irritation assessments predicted that **7a** poses no skin irritation risk and only mild ocular irritation, which is consistent with the safety profiles of other derivatives.

These findings suggest that **7a** possesses a favorable toxicity and safety profile, making it a promising VEGFR-2 inhibitor with a lower carcinogenic and mutagenic risk than sorafenib. Future studies should include *in vivo* toxicity evaluations and long-term safety assessments to confirm these computational predictions and ensure its suitability for clinical development.

2.3.9.1. Pharmacokinetic profiling study. A computational *in silico* analysis was carried out to assess the physicochemical characteristics and pharmacokinetic profiles of the synthesized compounds, using sorafenib as a reference. Drug molecules are more likely to exhibit good oral absorption if they meet at least three out of the four criteria outlined in Lipinski's rule of five: (1) no more than 5 hydrogen bond donors (OH, NH, SH), (2) no more than 10 hydrogen bond acceptors (N, O, S), (3) a molecular

Table 7 Predicted toxicity and safety profile of the nicotinamide–thiadiazol hybrids and sorafenib

Comp.	Ames prediction	Mouse-female FDA	DTP	Rat oral LD ₅₀ ^a	Rat chronic LOAEL ^a	Skin irritancy	Ocular irritancy
7a	Non-mutagen	Non-carcinogen	Non-toxic	0.531148	0.0618943	None	Mild
7b				0.247088	0.0276375		
7c				0.418376	0.049371		
7d				0.329557	0.0383128		
7e				0.353069	0.0303718		
7f				0.271895	0.034525		
7g	Mutagen	Single-carcinogen	Toxic	0.331188	0.0368119		
Sorafenib	Non-mutagen			0.822583	0.00482816		

^a Unit: g kg^{−1} body weight.

Table 8 Physicochemical properties of the synthesized molecules

Compound	Lipinski's rule of five					Veber's rule	
	log <i>P</i>	Mol. wt	HBD	HBA	Violation of Lipinski's rule	Number of rotatable bonds	TPSA
7a	4.258	490.965	1	8	0	6	124.68
7b	4.258	490.965	1	8	0	6	124.68
7c	4.08	470.546	1	8	0	6	124.68
7d	4.08	470.546	1	8	0	6	124.68
7g	4.566	484.573	1	8	0	6	124.68
Sorafenib	4.175	464.825	3	7	0	6	92.35

weight under 500 Da, and (4) a log *P* value below 5. Compounds that violate more than one of these rules are typically associated with poor oral bioavailability. Additionally, limited molecular flexibility—quantified by the number of rotatable bonds—and a low polar surface area have also been identified as key indicators of favorable oral bioavailability.⁴⁵ Specifically, molecules with 10 or fewer rotatable bonds and a polar surface area of 140 Å² or less are considered likely to be well absorbed. According to the data presented in Table 8, all the synthesized compounds, along with sorafenib, complied with both Lipinski's and Veber's guidelines.^{45,46}

3. Conclusion

This study demonstrates the potential of **7a** as a promising VEGFR-2 inhibitor with strong anticancer activity against breast cancer cells. The compound exhibited potent cytotoxic effects, inducing S-phase arrest and apoptosis, with significant activation of caspase-3 and upregulation of Bax, confirming its role in intrinsic apoptotic pathway activation. Additionally, VEGFR-2 inhibition assays revealed its high kinase inhibitory potential, comparable to the clinically approved inhibitor sorafenib. Computational studies, including molecular docking, MD simulations (200 ns), MM-GBSA, ProLIF, PCAT, and FEL analyses, further validated the strong and stable binding of **7a** to VEGFR-2. Moreover, ADMET predictions indicated good absorption, high plasma protein binding, and non-CYP2D6 inhibition, suggesting a favorable pharmacokinetic profile. Toxicity assessments classified **7a** as non-mutagenic and non-carcinogenic, with a lower predicted toxicity compared to sorafenib, highlighting its potential as a safer alternative. Furthermore, Density Functional Theory (DFT) calculations confirmed the structural stability and reactivity of **7a**, reinforcing its suitability as a lead candidate for further development. Given its potent anticancer activity, VEGFR-2 selectivity, and favorable safety profile, **7a** represents a strong candidate for further *in vivo* evaluation. Future studies should focus on preclinical validation, pharmacokinetic profiling, and structural modifications to enhance its efficacy and therapeutic potential, ultimately advancing it as a novel targeted anticancer agent.

4. Experimental

4.1. Chemistry

Standard chemical procedures were used to synthesize and characterize the target molecules. The ESI† include more details about the experimental procedures. Compounds **3**, **5**, and **6a–g** were obtained using the published procedures.^{30,47–50}

4.1.1. General procedure for the synthesis of the final compounds 7a–g. The hydrazone derivatives **6a–g** reacted with an equivalent quantity of compound **5** in 20 mL of absolute ethanol, utilizing 1 equivalent of TEA as a catalyst. All components were subjected to reflux for a duration of 6 hours. After the filtering and washing of the precipitates with hot ethanol, the final nicotinamide derivatives **7a–g** were obtained, respectively.

4.1.1.1. *N*-(4-((*E*)-1-(((*Z*)-5-Acetyl-3-(2-chlorophenyl)-1,3,4-thiadiazol-2(3*H*)-ylidene)hydrazono)ethyl)phenyl)nicotinamide **7a.**

Yellowish white powder (yield, 78%); mp = 205–207 °C; FT-IR (ν_{\max} , cm⁻¹): 3322 (NH), 3069, 3037 (C–H aromatic), 2998, 2939, 2877 (C–H aliphatic), 1677, 1657 (C=O); ¹H NMR (400 MHz, DMSO-*d*₆) δ 10.61 (s, 1H), 9.11 (dd, *J* = 2.4, 0.9 Hz, 1H), 8.76 (dd, *J* = 4.8, 1.7 Hz, 1H), 8.31–8.28 (m, 1H), 7.86 (d, *J* = 3.5 Hz, 4H), 7.81–7.75 (m, 2H), 7.62–7.56 (m, 3H), 2.52 (s, 3H), 2.20 (s, 3H); ¹³C NMR (101 MHz, DMSO-*d*₆) δ 199.70, 189.72, 164.26, 159.89, 152.30, 150.72, 148.78, 140.44, 135.66, 135.23, 132.82, 131.82, 131.17, 130.61, 130.22, 128.60, 127.27, 127.03, 123.65, 120.04, 120.01, 25.06, 14.82; mass (*m/z*): 490 (*M*⁺, 49.82%), 90 (100%, base peak); anal. calcd for C₂₄H₁₉ClN₆O₂S (490.97): C, 58.71; H, 3.90; N, 17.12. Found: C, 58.94; H, 4.06; N, 17.31%.

4.1.1.2. *N*-(4-((*E*)-1-(((*Z*)-5-Acetyl-3-(4-chlorophenyl)-1,3,4-thiadiazol-2(3*H*)-ylidene)hydrazono)ethyl)phenyl)nicotinamide **7b.** Yellowish white powder (yield, 75%); mp = 212–214 °C; HPLC purity 96%; FT-IR (ν_{\max} , cm⁻¹): 3398 (NH), 3061 (C–H aromatic), 2952, 2925, 2853 (C–H aliphatic), 1711, 1665 (C=O); ¹H NMR (400 MHz, DMSO-*d*₆) δ 10.61 (s, 1H), 9.13 (s, 1H), 8.77 (d, *J* = 4.8 Hz, 1H), 8.31 (dt, *J* = 8.0, 2.1 Hz, 1H), 8.18–8.09 (m, 2H), 7.94–7.84 (m, 4H), 7.69–7.62 (m, 2H), 7.58 (dd, *J* = 8.0, 4.8 Hz, 1H), 2.59 (s, 3H), 2.43 (s, 3H); ¹³C NMR (101 MHz, DMSO-*d*₆) δ 189.77, 164.21, 163.93, 160.26, 152.22, 151.01, 148.74, 140.55, 137.67, 135.56, 132.53, 131.02, 129.12, 127.11, 123.53, 123.36, 119.88, 25.05, 15.33; mass (*m/z*): 520 (*M*⁺, 44.02%), 387 (100%, base peak); anal. calcd for C₂₄H₁₉ClN₆O₂S (490.97): C, 58.71; H, 3.90; N, 17.12. Found: C, 58.55; H, 3.75; N, 17.43%.

4.1.1.3. *N*-(4-((*E*)-1-(((*Z*)-5-Acetyl-3-(*m*-tolyl)-1,3,4-thiadiazol-2(3*H*)-ylidene)hydrazono)ethyl)phenyl)nicotinamide **7c.** White powder (yield, 80%); mp = 197–199 °C; HPLC purity 100%; FT-IR (ν_{\max} , cm⁻¹): 3338 (NH), 2981, 2977, 2918 (C–H aliphatic), 1744, 1657 (C=O); ¹H NMR (400 MHz, DMSO-*d*₆) δ 10.61 (s, 1H), 9.13 (d, *J* = 2.3 Hz, 1H), 8.77 (dd, *J* = 4.9, 1.7 Hz, 1H), 8.31 (dt, *J* = 8.2, 2.1 Hz, 1H), 7.93–7.85 (m, 6H), 7.58 (dd, *J* = 8.0, 4.8 Hz, 1H), 7.45 (t, *J* = 7.8 Hz, 1H), 7.22 (d, *J* = 7.6 Hz, 1H), 2.58 (s, 3H), 2.41 (d, *J* = 1.7 Hz, 6H); ¹³C NMR (101 MHz, DMSO-*d*₆) δ 189.89, 164.32, 159.95, 152.30, 148.79, 140.50, 138.85, 138.75, 135.66, 132.75, 130.52, 129.01, 127.89, 127.12, 123.64, 122.50, 119.99, 119.23, 40.20, 25.11, 21.23, 15.26; mass (*m/z*): 470 (*M*⁺, 23.76%), 88 (100%, base peak); anal. calcd for C₂₅H₂₂N₆O₂S (470.55): C, 63.81; H, 4.71; N, 17.86. Found: C, 63.65; H, 4.85; N, 18.03%.

4.1.1.4. *N*-(4-((*E*)-1-(((*Z*)-5-Acetyl-3-(*p*-tolyl)-1,3,4-thiadiazol-2(3*H*)-ylidene)hydrazono)ethyl)phenyl)nicotinamide **7d.** White powder (yield, 80%); mp = 195–197 °C; HPLC purity 100%; FT-IR (ν_{\max} , cm⁻¹): 3333 (NH), 2971, 2869 (C–H aliphatic), 1736, 1680 (C=O); ¹H NMR (400 MHz, DMSO-*d*₆) δ 10.61 (s, 1H), 9.13 (d, *J* = 2.3 Hz, 1H), 8.77 (dd, *J* = 4.8, 1.7 Hz, 1H), 8.31 (dt, *J* = 8.1, 2.0 Hz, 1H), 7.95–7.87 (m, 6H), 7.58 (dd, *J* = 8.0, 4.8 Hz, 1H), 7.38 (d, *J* = 8.3 Hz, 2H), 2.57 (s, 3H), 2.40 (s, 3H), 2.38 (s, 3H); ¹³C NMR (101 MHz, DMSO-*d*₆) δ 189.71, 164.25, 164.19, 159.71, 152.21, 150.39, 148.74, 140.43, 136.76, 136.40, 135.54, 132.66, 130.45, 129.52, 127.02, 123.51, 122.04, 119.88, 25.01, 20.62, 15.18; mass (*m/z*): 470 (*M*⁺, 10.12%), 91 (100%, base peak); anal. calcd for C₂₅H₂₂N₆O₂S (470.55): C, 63.81; H, 4.71; N, 17.86. Found: C, 63.59; H, 4.85; N, 18.09%.

4.1.1.5. *N*-(4-((*E*)-1-(((*Z*)-5-Acetyl-3-(4-chloro-2-nitrophenyl)-1,3,4-thiadiazol-2(3*H*)-ylidene)hydrazono)ethyl)phenyl)



nicotinamide 7e. Yellowish powder (yield, 70%); mp = 185–187 °C; FT-IR (ν_{max} , cm^{-1}): 3248 (NH), 3003 (C–H aromatic), 2931, 2838 (C–H aliphatic), 1691, 1643 (C=O); ^1H NMR (400 MHz, $\text{DMSO}-d_6$) δ 10.60 (s, 1H), 9.12 (s, 1H), 8.76 (d, J = 4.3 Hz, 1H), 8.34 (d, J = 2.3 Hz, 1H), 8.30 (dt, J = 8.0, 2.0 Hz, 1H), 8.06 (dd, J = 8.7, 2.4 Hz, 1H), 7.99 (d, J = 8.6 Hz, 1H), 7.86 (s, 4H), 7.56 (dd, J = 7.9, 4.8 Hz, 1H), 2.55 (s, 3H), 2.20 (s, 3H); ^{13}C NMR (101 MHz, $\text{DMSO}-d_6$) δ 189.52, 164.22, 163.08, 160.72, 152.22, 152.01, 148.77, 144.21, 140.62, 135.56, 134.54, 134.02, 132.41, 130.45, 129.87, 128.99, 127.11, 125.43, 123.52, 119.85, 25.04, 14.68; mass (m/z): 535 (M^+ , 4.46%), 367 (100%, base peak); anal. calcd for $\text{C}_{24}\text{H}_{18}\text{ClN}_7\text{O}_4\text{S}$ (535.96): C, 53.78; H, 3.39; N, 18.29. Found: C, 53.91; H, 3.43; N, 18.50%.

4.1.1.6. *N*-(4-((*E*)-1-(((*Z*)-5-Acetyl-3-(4-nitrophenyl)-1,3,4-thiadiazol-2(3*H*)-ylidene)hydrazono)ethyl)phenyl)nicotinamide 7f. Orange powder (yield, 77%); mp = 190–192 °C; HPLC purity 100%; FT-IR (ν_{max} , cm^{-1}): 3256 (NH), 3046 (C–H aromatic), 2989, 2945, 2921 (C–H aliphatic), 1684, 1667 (C=O); ^1H NMR (400 MHz, $\text{DMSO}-d_6$) δ 10.66 (s, 1H), 9.15 (s, 1H), 8.83–8.77 (m, 1H), 8.48 (s, 4H), 8.33 (s, 1H), 7.97–7.90 (m, 4H), 7.61 (s, 1H), 2.66 (s, 3H), 2.60 (s, 3H); mass (m/z): 501 (M^+ , 31.99%), 267 (100%, base peak); anal. calcd for $\text{C}_{24}\text{H}_{19}\text{N}_7\text{O}_4\text{S}$ (501.52): C, 57.48; H, 3.82; N, 19.55. Found: C, 57.39; H, 4.06; N, 19.73%.

4.1.1.7. *N*-(4-((*E*)-1-(((*Z*)-5-Acetyl-3-(3,4-dimethylphenyl)-1,3,4-thiadiazol-2(3*H*)-ylidene)hydrazono)ethyl)phenyl)nicotinamide 7g. White powder (yield, 82%); mp = 195–197 °C; HPLC purity 100%; FT-IR (ν_{max} , cm^{-1}): 3420 (NH), 3057 (C–H aromatic), 2992, 2966, 2941 (C–H aliphatic), 1640 (C=O); ^1H NMR (400 MHz, $\text{DMSO}-d_6$) δ 10.60 (s, 1H), 9.12 (d, J = 2.3 Hz, 1H), 8.77 (dd, J = 4.9, 1.6 Hz, 1H), 8.31 (dt, J = 8.1, 2.0 Hz, 1H), 7.86 (s, 4H), 7.81 (d, J = 2.4 Hz, 1H), 7.73 (dd, J = 8.2, 2.4 Hz, 1H), 7.57 (dd, J = 8.0, 4.8 Hz, 1H), 7.29 (d, J = 8.3 Hz, 1H), 2.54 (s, 3H), 2.37 (s, 3H), 2.29 (s, 3H), 2.26 (s, 3H); ^{13}C NMR (101 MHz, $\text{DMSO}-d_6$) δ 189.68, 164.24, 164.18, 159.59, 152.22, 150.22, 148.75, 140.42, 137.06, 136.63, 135.55, 135.43, 132.67, 130.45, 129.85, 126.99, 123.52, 122.85, 119.85, 119.35, 24.97, 19.68, 19.00, 15.10; mass (m/z): 484 (M^+ , 1.89%), 414 (100%, base peak); anal. calcd for $\text{C}_{26}\text{H}_{24}\text{N}_6\text{O}_2\text{S}$ (484.58): C, 64.44; H, 4.99; N, 17.34. Found: C, 64.27; H, 5.12; N, 17.48%.

4.2. In vitro studies

4.2.1. Cytotoxicity. The cytotoxicity and selectivity of the synthesized compounds (7a–7g) were tested against MDA-MB-231, MCF-7, WI-38, and WISH cell lines using the MTT assay.^{51,52} The reference drug was also evaluated. Detailed methods are available in the ESI.†

4.2.2. Enzyme inhibition. The inhibitory potential of 7a and sorafenib against VEGFR-2 was tested using enzyme assay kits across a concentration range of 0.3–1000 nM.⁵³ The procedure is described in the ESI.†

4.2.3. ELISA assay for BAX, Bcl-2, and caspase-3. The expression of apoptosis-related genes (BAX, Bcl-2, and caspase-3) in MDA-MB-231 cells treated with 7a was measured using ELISA technique, following established protocols.⁵⁴ Detailed methods are available in the ESI.†

4.2.4. Flow cytometry. Flow cytometry was used to examine the effects of 7a on apoptosis and cell cycle progression in MDA-MB-231 cells.⁵⁵ Further details can be found in the ESI.†

4.3. Computational studies

4.3.1. Molecular docking. Molecular docking simulations were performed to study the interactions of the synthesized nicotinamide–thiadiazole hybrids (7a–7g) with VEGFR-2 (PDB ID 4ASD) as presented in the ESI.†^{50,56}

4.3.2. MD simulations. MD simulations were conducted on the VEGFR-2–7a complex using the CHARMM-GUI web server and GROMACS 2021 software.^{57,58} The binding free energy of 7a was estimated using the gmx_MMPBSA tool with the MM-GBSA method. Principal component analysis (PCA) was applied to evaluate dynamic motions of alpha carbons in specific protein regions. The free energy landscape (FEL) was explored by analyzing two states connected through their probabilities using an exponential relationship.^{59,60} Detailed protocols are provided in the ESI.†

4.3.3. ADMET and toxicity. The pharmacokinetic properties and toxicity risks of the nicotinamide–thiadiazole hybrids (7a–7g) were predicted using Discovery Studio 4.0 software.⁶¹ Details are provided in the ESI.†

4.3.4. Density functional theory (DFT). Structural optimization and reactivity analysis for compound 7a were performed using Gaussian 09 software, employing the DFT method with the B3LYP functional and the 6-31+G(d,p) basis set.⁵⁶ Additional methods are detailed in the ESI.†

Data availability

Data are available with corresponding authors upon request.

Conflicts of interest

The authors confirm that they have no conflicts of interest to disclose.

Acknowledgements

This research was funded by Princess Nourah bint Abdulrahman University Researchers Supporting Project number (PNURSP2025R142), Princess Nourah bint Abdulrahman University, Riyadh, Saudi Arabia. The authors thank Research Center at AlMaarefa University for funding this work.

References

- 1 L. Wilkinson and T. Gathani, Understanding breast cancer as a global health concern, *Brit. J. Radiol.*, 2022, **95**(1130), 20211033.
- 2 S. M. Schwartz, Epidemiology of Cancer, *Clin. Chem.*, 2024, **70**(1), 140–149.
- 3 A. A. Shah, M. A. Kamal and S. Akhtar, Tumor Angiogenesis and VEGFR-2: Mechanism, Pathways and Current Biological



- Therapeutic Interventions, *Curr. Drug Metab.*, 2021, **22**(1), 50–59.
- 4 E. B. Elkaeed, R. G. Yousef, H. Elkady, A. B. Mehany, B. A. Alsouk, D. Z. Husein, I. M. Ibrahim, A. M. Metwaly and I. H. Eissa, In silico, in vitro VEGFR-2 inhibition, and anticancer activity of a 3-(hydrazonomethyl) naphthalene-2-ol derivative, *J. Biomol. Struct. Dyn.*, 2023, **41**(16), 7986–8001.
 - 5 M. S. Taghour, H. Elkady, W. M. Eldehna, N. El-Deeb, A. M. Kenawy, A. E. Abd El-Wahab, E. B. Elkaeed, B. A. Alsouk, A. M. Metwaly and I. H. Eissa, Discovery of new quinoline and isatine derivatives as potential VEGFR-2 inhibitors: design, synthesis, antiproliferative, docking and MD simulation studies, *J. Biomol. Struct. Dyn.*, 2023, **41**(21), 11535–11550.
 - 6 I. H. Eissa, R. G. Yousef, H. Elkady, E. B. Elkaeed, A. A. Alsouk, D. Z. Husein, I. M. Ibrahim, M. A. Elhendawy, M. Godfrey and A. M. Metwaly, Design, semi-synthesis, anti-cancer assessment, docking, MD simulation, and DFT studies of novel theobromine-based derivatives as VEGFR-2 inhibitors and apoptosis inducers, *Comput. Biol. Chem.*, 2023, **107**, 107953.
 - 7 X. J. Liu, H. C. Zhao, S. J. Hou, H. J. Zhang, L. Cheng, S. Yuan, L. R. Zhang, J. Song, S. Y. Zhang and S. W. Chen, Recent development of multi-target VEGFR-2 inhibitors for the cancer therapy, *Bioorg. Chem.*, 2023, **133**, 106425.
 - 8 T. Arao, K. Matsumoto, K. Furuta, K. Kudo, H. Kaneda, T. Nagai, K. Sakai, Y. Fujita, D. Tamura, K. Aomatsu, F. Koizumi and K. Nishio, Acquired drug resistance to vascular endothelial growth factor receptor 2 tyrosine kinase inhibitor in human vascular endothelial cells, *Anticancer Res.*, 2011, **31**(9), 2787–2796.
 - 9 Q. Li, K. Chen, T. Zhang, D. Jiang, L. Chen, J. Jiang, C. Zhang and S. Li, Understanding sorafenib-induced ferroptosis and resistance mechanisms: implications for cancer therapy, *Eur. J. Pharmacol.*, 2023, **955**, 175913.
 - 10 L. Cosmai, M. Gallieni, W. Liguigli and C. Porta, Renal toxicity of anticancer agents targeting vascular endothelial growth factor (VEGF) and its receptors (VEGFRs), *J. Nephrol.*, 2017, **30**(2), 171–180.
 - 11 S. Lai, A. Molino, P. Seminara, F. Longo, G. Innico, B. Coppola, D. Mastroluca, A. Galani, M. Dimko, P. Aceto and C. Lai, Vascular Endothelial Growth Factor Inhibitor Therapy and Cardiovascular and Renal Damage in Renal Cell Carcinoma, *Curr. Vasc. Pharmacol.*, 2018, **16**(2), 190–196.
 - 12 S. Lai, M. I. Amabile, S. Mazzaferro, A. P. Mitterhofer, A. Mazzarella, A. Galani, G. Imbimbo, R. Cianci, M. Pasquali and A. Molino, Effects of sunitinib on endothelial dysfunction, metabolic changes, and cardiovascular risk indices in renal cell carcinoma, *Cancer Med.*, 2020, **9**(11), 3752–3757.
 - 13 A. A. Abdelgalil, H. M. Alkahtani and F. I. Al-Jenoobi, Sorafenib, *Profiles of Drug Substances, Excipients, and Related Methodology*, 2019, vol. 44, pp. 239–266.
 - 14 A. M. Metwaly, M. A. Abu-Saied, I. M. Gobaara, A. M. Lotfy, B. A. Alsouk, E. B. Elkaeed and I. H. Eissa, Nicotinamide Loaded Chitosan Nanocomplex Shows Improved Anticancer Potential: Molecular Docking, Synthesis, Characterization and In vitro Evaluations, *Curr. Org. Chem.*, 2024, **28**(1), 46–55.
 - 15 M. Szeliga, Thiadiazole derivatives as anticancer agents, *Pharmacol. Rep.*, 2020, **72**(5), 1079–1100.
 - 16 S. Grimme and P. R. Schreiner, Computational Chemistry: The Fate of Current Methods and Future Challenges, *Angew. Chem., Int. Ed. Engl.*, 2018, **57**(16), 4170–4176.
 - 17 A. Varnek and I. I. Baskin, Chemoinformatics as a Theoretical Chemistry Discipline, *Mol. Inform.*, 2011, **30**(1), 20–32.
 - 18 S. A. Hollingsworth and R. O. Dror, Molecular Dynamics Simulation for All, *Neuron*, 2018, **99**(6), 1129–1143.
 - 19 A. M. Metwaly, E. M. El-Fakharany, A. A. Alsouk, I. M. Ibrahim, E. B. Elkaeed and I. H. Eissa, Integrated study of Quercetin as a potent SARS-CoV-2 RdRp inhibitor: Binding interactions, MD simulations, and In vitro assays, *PLoS One*, 2024, **19**(12), e0312866.
 - 20 L. L. G. Ferreira and A. D. Andricopulo, ADMET modeling approaches in drug discovery, *Drug Discov. Today*, 2019, **24**(5), 1157–1165.
 - 21 A. M. Metwaly, M. S. Alesawy, B. A. Alsouk, I. M. Ibrahim, E. B. Elkaeed and I. H. Eissa, Computer-Assisted Drug Discovery of Potential African Anti-SARS-CoV-2 Natural Products Targeting the Helicase Protein, *Nat. Prod. Commun.*, 2024, **19**(4), 1–23.
 - 22 A. L. Jenner, R. A. Aogo, C. L. Davis, A. M. Smith and M. Craig, Leveraging Computational Modeling to Understand Infectious Diseases, *Curr. Pathobiol. Rep.*, 2020, **8**(4), 149–161.
 - 23 M. M. Ahmed, M. E.-F. Esmail, A. A. Aisha, M. I. Ibrahim, B. E. Eslam and H. E. Ibrahim, Integrated in Silico and in Vitro Studies of Rutin's Potential against SARS-CoV-2 through the Inhibition of the RNA-dependent RNA Polymerase, *Curr. Med. Chem.*, 2025, **32**, 1–27.
 - 24 U. Gupta and D. Paliwal, Discovery, current trends in computational chemistry for breast cancer, *Lett. Drug Des. Discov.*, 2023, **20**(1), 2–15.
 - 25 A. M. Metwaly, H. Abd-El-Azim, M. Zewail, A. A. Alsouk, E. B. Elkaeed and I. H. Eissa, Chitosomal Encapsulation Enhances the Anticancer Efficacy of a Theobromine Analogue: An Integrated In Silico and In Vitro Study, *J. Comput. Biophys. Chem.*, 2025, 557–573, 1–17.
 - 26 I. H. Eissa, R. G. Yousef, M. Sami, E. B. Elkaeed, B. A. Alsouk, I. M. Ibrahim, D. Z. Husein, H. Elkady and A. M. Metwaly, Exploring the anticancer properties of a new nicotinamide analogue: investigations into in silico analysis, antiproliferative effects, selectivity, VEGFR-2 inhibition, apoptosis induction, and migration suppression, *Pathol., Res. Pract.*, 2023, **252**, 154924.
 - 27 I. H. Eissa, M. A. E. Bkrah, R. G. Yousef, H. Elkady, E. B. Elkaeed, B. A. Alsouk, I. M. Ibrahim, A. M. Metwaly and D. Z. Husein, Design and In Silico and In Vitro Evaluations of a Novel Nicotinamide Derivative as a VEGFR-2 Inhibitor, *J. Chem.*, 2024, **2024**(1), 2176512.
 - 28 R. G. Yousef, H. Elkady, E. B. Elkaeed, I. M. M. Gobaara, H. A. Al-Ghulikah, D. Z. Husein, I. M. Ibrahim, A. M. Metwaly and I. H. Eissa, (E)-N-(3-(1-(2-(4(2,2,2-



- Trifluoroacetamido)benzoyl)hydrazono)ethyl)phenyl) nicotinamide: A Novel Pyridine Derivative for Inhibiting Vascular Endothelial Growth Factor Receptor-2: Synthesis, Computational, and Anticancer Studies, *Molecules*, 2022, 27(22), 7719–7743.
- 29 H. Elkady, W. E. Elgammal, H. A. Mahdy, S. Zara, S. Carradori, D. Z. Husein, A. A. Alsouk, I. M. Ibrahim, E. B. Elkaeed, A. M. Metwaly and I. H. Eissa, Anti-proliferative 2,3-dihydro-1,3,4-thiadiazoles targeting VEGFR-2: design, synthesis, in vitro, and in silico studies, *Comput. Biol. Chem.*, 2024, **113**, 108221.
 - 30 I. H. Eissa, H. Elkady, W. E. Elgammal, H. A. Mahdy, E. B. Elkaeed, A. A. Alsouk, I. M. Ibrahim, D. Z. Husein and A. M. Metwaly, Integrated in silico and in vitro discovery of a new anticancer thiadiazole analog targeting VEGFR-2, *J. Mol. Struct.*, 2024, **1312**, 138641.
 - 31 I. H. Eissa, W. E. Elgammal, H. A. Mahdy, S. Zara, S. Carradori, D. Z. Husein, M. N. Alharthi, I. M. Ibrahim, E. B. Elkaeed, H. Elkady and A. M. Metwaly, Design, synthesis, and evaluation of novel thiadiazole derivatives as potent VEGFR-2 inhibitors: a comprehensive in vitro and in silico study, *RSC Adv.*, 2024, **14**(48), 35505–35519.
 - 32 W. E. Elgammal, H. Elkady, H. A. Mahdy, D. Z. Husein, A. A. Alsouk, B. A. Alsouk, I. M. Ibrahim, E. B. Elkaeed, A. M. Metwaly and I. H. Eissa, Rationale design and synthesis of new apoptotic thiadiazole derivatives targeting VEGFR-2: computational and in vitro studies, *RSC Adv.*, 2023, **13**(51), 35853–35876.
 - 33 M. M. Alanazi, H. Elkady, N. A. Alsaif, A. J. Obaidullah, W. A. Alanazi, A. M. Al-Hossaini, M. A. Alharbi, I. H. Eissa and M. A. Dahab, Discovery of new quinoxaline-based derivatives as anticancer agents and potent VEGFR-2 inhibitors: design, synthesis, and in silico study, *J. Mol. Struct.*, 2021, 132220.
 - 34 M. M. Alanazi, H. Elkady, N. A. Alsaif, A. J. Obaidullah, H. M. Alkahtani, M. M. Alanazi, M. A. Alharbi, I. H. Eissa and M. A. Dahab, New quinoxaline-based VEGFR-2 inhibitors: design, synthesis, and antiproliferative evaluation with in silico docking, ADMET, toxicity, and DFT studies, *RSC Adv.*, 2021, **11**(48), 30315–30328.
 - 35 R. G. Yousef, H. M. Sakr, I. H. Eissa, A. B. Mehany, A. M. Metwaly, M. A. Elhendawy, M. M. Radwan, M. A. ElSohly, H. S. Abulkhair and K. El-Adl, New quinoxaline-2 (1 H)-ones as potential VEGFR-2 inhibitors: design, synthesis, molecular docking, ADMET profile and anti-proliferative evaluations, *New J. Chem.*, 2021, **45**(36), 16949–16964.
 - 36 I. H. Eissa, R. G. Yousef, H. Elkady, E. B. Elkaeed, A. A. Alsouk, D. Z. Husein, I. M. Ibrahim, M. A. Elhendawy, M. Godfrey and A. M. Metwaly, Identification of new theobromine-based derivatives as potent VEGFR-2 inhibitors: design, semi-synthesis, biological evaluation, and in silico studies, *RSC Adv.*, 2023, **13**(33), 23285–23307.
 - 37 R. G. Yousef, I. H. Eissa, H. Elkady, A. B. M. Mehany, M. A. Abo-Saif, M. M. Radwan, M. A. ElSohly, I. M. Ibrahim, A. Elwan and M. A. El-Zahabi, Design and synthesis of new nicotinamides as immunomodulatory VEGFR-2 inhibitors and apoptosis inducers, *Future Med. Chem.*, 2024, 1–16.
 - 38 R. G. Yousef, H. Elkady, E. B. Elkaeed, I. M. Gobaara, H. A. Al-Ghulikah, D. Z. Husein, I. M. Ibrahim, A. M. Metwaly and I. H. Eissa, (E)-N-(3-(1-(2-(4-(2, 2, 2-Trifluoroacetamido) benzoyl) hydrazono) ethyl) phenyl) nicotinamide: A Novel Pyridine Derivative for Inhibiting Vascular Endothelial Growth Factor Receptor-2: Synthesis, Computational, and Anticancer Studies, *Molecules*, 2022, 27(22), 7719.
 - 39 B. W. Matore, P. P. Roy and J. Singh, Discovery of novel VEGFR2-TK inhibitors by phthalimide pharmacophore based virtual screening, molecular docking, MD simulation and DFT, *J. Biomol. Struct. Dyn.*, 2023, **41**(22), 13056–13077.
 - 40 P. J. Chaudhari, A. R. Nemade and A. A. Shirkhedkar, Recent updates on potential of VEGFR-2 small-molecule inhibitors as anticancer agents, *RSC Adv.*, 2024, **14**(45), 33384–33417.
 - 41 I. Fleming, *Molecular Orbitals and Organic Chemical Reactions*, John Wiley & Sons, 2011.
 - 42 T. Yoshida and S. Hirono, A 3D-QSAR analysis of CDK2 inhibitors using FMO calculations and PLS regression, *Chem. Pharm. Bull.*, 2019, **67**(6), 546–555.
 - 43 S. A. El-Metwally, H. Elkady, M. Hagrass, D. Z. Husein, I. M. Ibrahim, M. S. Taghour, H. A. El-Mahdy, A. Ismail, B. A. Alsouk and E. B. Elkaeed, Design, synthesis, anti-proliferative evaluation, docking, and MD simulation studies of new thieno [2, 3-d] pyrimidines targeting VEGFR-2, *RSC Adv.*, 2023, **13**(33), 23365–23385.
 - 44 H. Elkady, O. A. El-Dardir, A. Elwan, M. S. Taghour, H. A. Mahdy, M. A. Dahab, E. B. Elkaeed, B. A. Alsouk, I. M. Ibrahim and D. Z. Husein, Synthesis, biological evaluation and computer-aided discovery of new thiazolidine-2, 4-dione derivatives as potential antitumor VEGFR-2 inhibitors, *RSC Adv.*, 2023, **13**(40), 27801–27827.
 - 45 D. F. Veber, S. R. Johnson, H.-Y. Cheng, B. R. Smith, K. W. Ward and K. D. Kopple, Molecular properties that influence the oral bioavailability of drug candidates, *J. Med. Chem.*, 2002, **45**(12), 2615–2623.
 - 46 C. A. Lipinski, F. Lombardo, B. W. Dominy and P. J. Feeney, Experimental and computational approaches to estimate solubility and permeability in drug discovery and development settings, *Adv. Drug Deliv. Rev.*, 2012, **64**, 4–17.
 - 47 W. E. Elgammal, H. Elkady, H. A. Mahdy, D. Z. Husein, A. A. Alsouk, B. A. Alsouk, I. M. Ibrahim, E. B. Elkaeed, A. M. Metwaly and I. H. Eissa, Rationale design and synthesis of new apoptotic thiadiazole derivatives targeting VEGFR-2: computational and in vitro studies, *RSC Adv.*, 2023, **13**(51), 35853–35876.
 - 48 H. Elkady, W. E. Elgammal, H. A. Mahdy, S. Zara, S. Carradori, D. Z. Husein, A. A. Alsouk, I. M. Ibrahim, E. B. Elkaeed and A. M. Metwaly, Anti-proliferative 2, 3-dihydro-1, 3, 4-thiadiazoles targeting VEGFR-2: design, synthesis, in vitro, and in silico studies, *Comput. Biol. Chem.*, 2024, **113**, 108221.
 - 49 H. A. Mahdy, H. Elkady, W. E. Elgammal, E. B. Elkaeed, A. A. Alsouk, I. M. Ibrahim, D. Z. Husein, M. A. Elkady, A. M. Metwaly and I. H. Eissa, Design, synthesis, in vitro,



- and in silico studies of new thiadiazol derivatives as promising VEGFR-2 inhibitors and apoptosis inducers, *J. Mol. Struct.*, 2024, 139019.
- 50 I. H. Eissa, W. E. Elgammal, H. A. Mahdy, S. Zara, S. Carradori, D. Z. Husein, M. N. Alharthi, I. M. Ibrahim, E. B. Elkaeed and H. Elkady, Design, synthesis, and evaluation of novel thiadiazole derivatives as potent VEGFR-2 inhibitors: a comprehensive in vitro and in silico study, *RSC Adv.*, 2024, **14**(48), 35505–35519.
 - 51 A. R. Kotb, D. A. Bakhotmah, A. E. Abdallah, H. Elkady, M. S. Taghour, I. H. Eissa and M. A. El-Zahabi, Design, synthesis, and biological evaluation of novel bioactive thalidomide analogs as anticancer immunomodulatory agents, *RSC Adv.*, 2022, **12**(52), 33525–33539.
 - 52 A. R. Kotb, A. E. Abdallah, H. Elkady, I. H. Eissa, M. S. Taghour, D. A. Bakhotmah, T. M. Abdelghany and M. A. El-Zahabi, Design, synthesis, anticancer evaluation, and in silico ADMET analysis of novel thalidomide analogs as promising immunomodulatory agents, *RSC Adv.*, 2023, **13**(16), 10488–10502.
 - 53 H. A. Mahdy, H. Elkady, M. S. Taghour, A. Elwan, M. A. Dahab, M. A. Elkady, E. G. Elsakka, E. B. Elkaeed, B. A. Alsouk and I. M. Ibrahim, New theobromine derivatives inhibiting VEGFR-2: design, synthesis, antiproliferative, docking and molecular dynamics simulations, *Future Med. Chem.*, 2023, **15**(14), 1233–1250.
 - 54 H. Qin and E. N. Benveniste, ELISA methodology to quantify astrocyte production of cytokines/chemokines in vitro, *Astrocytes: Methods and Protocols*, 2012, pp. 235–249.
 - 55 Z. Darzynkiewicz, E. Bedner and P. Smolewski, Flow cytometry in analysis of cell cycle and apoptosis, *Seminars in Hematology*, Elsevier, 2001, pp. 179–193.
 - 56 D. S. Biovia, Discovery studio modeling environment, *Release*, San Diego, CA, 2017.
 - 57 B. R. Brooks, C. L. Brooks III, A. D. Mackerell Jr, L. Nilsson, R. J. Petrella, B. Roux, Y. Won, G. Archontis, C. Bartels and S. Boresch, CHARMM: the biomolecular simulation program, *J. Comput. Chem.*, 2009, **30**(10), 1545–1614.
 - 58 S. Jo, X. Cheng, S. M. Islam, L. Huang, H. Rui, A. Zhu, H. S. Lee, Y. Qi, W. Han and K. Vanommeslaeghe, CHARMM-GUI PDB manipulator for advanced modeling and simulations of proteins containing nonstandard residues, *Adv. Protein Chem. Struct. Biol.*, 2014, **96**, 235–265.
 - 59 T. Tuccinardi, What is the current value of MM/PBSA and MM/GBSA methods in drug discovery?, *Expet Opin. Drug Discov.*, 2021, **16**(11), 1233–1237.
 - 60 M. S. Valdés-Tresanco, M. E. Valdés-Tresanco, P. A. Valiente and E. Moreno, gmx_MMPBSA: a new tool to perform end-state free energy calculations with GROMACS, *J. Chem. Theor. Comput.*, 2021, **17**(10), 6281–6291.
 - 61 A. M. Metwaly, E. B. Elkaeed, B. A. Alsouk, A. M. Saleh, A. E. Mostafa and I. H. Eissa, The Computational Preventive Potential of the Rare Flavonoid, Patuletin, Isolated from *Tagetes patula*, against SARS-CoV-2, *Plants*, 2022, **11**(14), 1886–1905.

